

## Atmospheric turbulence observed during a fuel-bed-scale low intensity surface fire

Joseph Seitz <sup>1</sup>, Shiyuan Zhong <sup>1\*</sup>, Joseph J. Charney <sup>2</sup>, Warren E. Heilman <sup>2,\*</sup>, Kenneth L. Clark <sup>3</sup>, Xindi Bian <sup>2</sup>, Nicholas S. Skowronski <sup>4</sup>, Michael R. Gallagher <sup>3</sup>, Matthew Patterson <sup>4</sup>, Jason Cole <sup>5</sup>, Michael T. Kiefer <sup>1</sup>, Rory Hadden <sup>6</sup>, and Eric Mueller <sup>6</sup>

<sup>1</sup> Department of Geography, Environment and Spatial Sciences, Michigan State University, East Lansing, MI 48824; [seitzjos@msu.edu](mailto:seitzjos@msu.edu) (J.S.); [mtkiefer@msu.edu](mailto:mtkiefer@msu.edu) (M.K.); [zhongs@msu.edu](mailto:zhongs@msu.edu) (S.Z.)

<sup>2</sup> USDA Forest Service, Northern Research Station, ~~3101 Discovery Dr~~ 2601 Coolidge Rd., Suite 203F, East Lansing, MI 48910; [joseph.j.charney@usda.gov](mailto:joseph.j.charney@usda.gov) (J.J.C.); [warren.heilman@usda.gov](mailto:warren.heilman@usda.gov) (W.H.); [xindi.bian@usda.gov](mailto:xindi.bian@usda.gov) (X.B.)

<sup>3</sup> USDA Forest Service, Northern Research Station, Silas Little Experimental Forest, 501 Four Mile Road, New Lisbon, NJ 08064; [kenneth.clark@usda.gov](mailto:kenneth.clark@usda.gov) (K.C.); [michael.r.gallagher@usda.gov](mailto:michael.r.gallagher@usda.gov) (M.G.)

<sup>4</sup> USDA Forest Service, Northern Research Station, 180 Canfield Street, Morgantown, WV 26505; [nicholas.s.skowronski@usda.gov](mailto:nicholas.s.skowronski@usda.gov) (N.S.); [matthew.m.patterson@usda.gov](mailto:matthew.m.patterson@usda.gov) (M.P.)

<sup>5</sup> USDA Forest Service, Northern Research Station, 5 Moon Library, 1 Forestry Dr., Syracuse NY 13210; [jason.cole2@usda.gov](mailto:jason.cole2@usda.gov) (J.C.)

<sup>6</sup> The University of Edinburgh, Edinburgh, EH9, 3FB, UK; [e.mueller@ed.ac.uk](mailto:e.mueller@ed.ac.uk) (E.M.); [r.hadden@ed.ac.uk](mailto:r.hadden@ed.ac.uk) (R.H.)

\* Correspondence to: Shiyuan Zhong, [zhongs@msu.edu](mailto:zhongs@msu.edu); Tel.: +1-517-432-4743

Received: date; Accepted: date; Published: date

1 **Abstract.** The ambient atmospheric environment affects the growth and spread of wildland fires,  
2 whereas heat and moisture release from the fires and the reduction of the surface drag in the  
3 burned areas can significantly alter local atmospheric conditions. Observational studies on fire-  
4 atmosphere interactions have used instrumented towers to collect data during prescribed fires,  
5 but a few towers in an operational scale burn plot (usually  $> 10^3 \text{ m}^2$ ) have made it extremely  
6 challenging to capture the myriad of factors controlling fire-atmosphere interactions, many of  
7 which exhibit strong spatial variability. Here, we present analyses of atmospheric turbulence data  
8 collected using a  $4 \times 4$  array of fast-response sonic anemometers during a fire experiment on a  $10$   
9  $\text{m} \times 10 \text{ m}$  burn plot. In addition to confirming some of the previous findings on atmospheric  
10 turbulence associated with low-intensity surface fires, our results revealed substantial  
11 heterogeneity in turbulent intensity and heat and momentum fluxes just above the combustion  
12 zone. Despite the small plot ( $100 \text{ m}^2$ ), fire-induced atmospheric turbulence exhibited strong  
13 dependence on the downwind distance from the initial line fire and the relative position specific  
14 to the fire front as the surface fire spread through the burn plot. This result highlights the  
15 necessity for coupled atmosphere-fire behavior models to have 1-2 m grid spacing to resolve  
16 heterogeneities in fire-atmosphere interactions that operate on spatiotemporal scales relevant to  
17 atmospheric turbulence. The findings here have important implications for modeling smoke  
18 dispersion, as atmospheric dispersion characteristics in the vicinity of a wildland fire are directly  
19 affected by fire-induced turbulence.

20

21

## 22 1 Introduction

23 Wildland fires are ~~directly affected by~~ fundamentally linked to atmospheric conditions,  
24 with Mm macroscale (thousands of kilometers, weeks to months) ~~atmospheric conditions factors,~~  
25 such as prolonged periods without substantial precipitation, high temperature, and low humidity,  
26 contribute to the ~~that~~ drying out and pre-heating of fuels, ~~often setting background the stage~~ for  
27 large wildland fires episodes (Potter, 1996; 2012; Finney *et al.*, 2015; Littell *et al.*, 2016;  
28 Kitzberger *et al.*, 2017). Once ignited, ~~fire behavior characteristics (e.g., burn intensity, ember~~  
29 ~~production, spotting, fire whirls and the rate of spread) are influenced more by~~ microscale (<  
30 1000 m, < 1 h) conditions, such as local topography and wind speed and direction, take  
31 precedence in shaping fire behavior characteristics like burn intensity, ember production,  
32 spotting, fire whirls and the rate of spread at the location of the fires. Most wildland fires tend to  
33 spread in the direction the wind blows, ~~and the~~ with stronger ~~the~~ wind speeds corresponding to the  
34 faster ~~the~~ fire spreads (Carrier *et al.*, 1991; Wolff *et al.*, 1991; Clark *et al.*, 1996). ~~Another~~  
35 ~~essential microscale factor affecting fire behavior is atmospheric turbulence, defined as irregular~~  
36 ~~microscale air motions in the forms of eddies that are superimposed on mean atmospheric~~  
37 ~~motions (Stull, 1988).~~

38 An essential microscale factor influencing fire behavior is atmospheric turbulence,  
39 characterized by irregular microscale air motions in the form of eddies superimposed on mean  
40 atmospheric motions (Stull, 1988). Turbulent eddies affect fire behavior as well as the transfer of  
41 gaseous and particulate emissions from the fires to the surrounding atmosphere (Clements *et al.*,  
42 2008; Seto *et al.*, 2014; Viegas and Neto, 2015; Skowonski and Hom, 2015; Heilman *et al.*,  
43 2015; Heilman, 2021). Turbulence in the atmosphere is generated primarily by wind shear as a  
44 result of changes in wind speed and/or direction, known as mechanical turbulence, and by

45 convection, referred to as thermal turbulence. Mechanical turbulence is often generated when air  
46 flow encounters surface drag, rough terrain or other natural or man-made obstacles and  
47 boundaries separating different air masses (e.g., weather fronts), different land cover types (e.g.,  
48 grass vs. forested land) or land use types (e.g., agriculture vs. urban). Thermal turbulence is  
49 produced when heated surface air rises ~~up~~ in the atmosphere, a process known as convection,  
50 ~~which~~ commonly occurings during daytime when incoming solar radiation ~~absorbed by the~~  
51 ~~earth's surface~~ exceeds outgoing terrestrial radiation. Fire-induced turbulence, ~~is~~ a type of  
52 thermal turbulence, ~~in that~~results from heat released by combustion, ~~produc~~inges buoyant plumes  
53 that rise ~~up~~ from the combustion zone.

54 Atmospheric turbulence is a pivotal factor influencing fire behavior and the complex  
55 exchange of momentum and scalars (e.g., heat, moisture, carbon monoxide, carbon dioxide, and  
56 particulate matter) between the combustion zone and the surrounding atmosphere. Existing  
57 literature on fire-induced turbulence predominantly draws from data gathered in either  
58 management-scale burns, encompassing plots ranging from several to hundreds of hectares, or  
59 fine-scale laboratory experiments conducted in burn chambers or wind tunnels under controlled  
60 conditions. Notably, a discernible gap exists in observations that seamlessly bridge these two  
61 scales (Skwonski, *et al.*, 2021). This study aims to fill this knowledge void by presenting a  
62 comprehensive analysis of turbulent data collected from a densely instrumented small-scale (10  
63 m x 10 m) burn plot situated in a pitch and loblolly pine plantation. Through this investigation,  
64 we seek to augment our understanding of how surface fires modify turbulence and contribute to  
65 the dynamic exchange of momentum and scalars between the fire and the surrounding  
66 atmosphere.

67 ~~Despite the important role atmospheric turbulence plays in fire behavior and in the~~  
68 ~~exchanges of momentum and scalars (e.g., heat, moisture, carbon monoxide, carbon dioxide~~  
69 ~~particulate matter or PM) between the combustion zone and the surrounding atmosphere,~~  
70 ~~detailed~~Comprehensive observations of atmosphere turbulence in the presence of wildland fires  
71 have only become available in recent decades. For instance, ~~the first large-scale field experiment~~  
72 ~~where comprehensive turbulence data were collected above and in the vicinity of a wildland fire~~  
73 ~~front was the~~ FireFlux experiment, conducted on February 23, 2006 over a 40-hectare plot of  
74 native tall-grass prairie in Galveston, Texas represented a significant large-scale field experiment  
75 where comprehensive turbulence data were collected above and in the vicinity of a wildland fire  
76 front (Clements *et al.*, 2007; Clements *et al.*, 2008). ~~Fire-atmosphere interactions were monitored~~  
77 ~~primarily using~~ The experiment utilized fast-response three-dimensional (3D) sonic  
78 anemometers mounted at multiple levels on a tall (43 m) and a short (10 m) tower within the  
79 burn plot. ~~This data-groundbreaking experiment~~ revealed a fivefold increase in turbulence  
80 kinetic energy and a threefold increase in surface stress during the fire-front passage, ~~and with a~~  
81 rapid return of turbulence to the ambient level ~~behind~~ the fire front. A ~~follow-up~~subsequent  
82 field experiment, ~~known as~~ FireFlux-II, took place at the same site in 2013, aiming with more  
83 measurements designed to fill gaps in the original FireFlux experiment and provide ~~further~~  
84 ~~information~~additional insight on fire-atmosphere interactions and fire-induced turbulence  
85 regimes (Clements *et al.*, 2019). ~~The data from FireFlux II have been used to validate fire~~  
86 ~~behavior models (Moody et al., 2022), but the results on the intensive collection of turbulence~~  
87 ~~data from FireFlux II are yet to be reported in the peer-reviewed literature.~~

88 While these ~~FireFlux and FireFlux II~~ experiments in Texas provided direct turbulence  
89 measurements during intense grass fires, ~~a number of other~~ wildland fire experiments in the New

90 Jersey Pine Barrens provided information on fire-induced turbulence during low-intensity forest  
91 understory fires (Heilman *et al.* 2015, 2017, 2019 and 2021; Mueller *et al.* 2017, 2019; Clark *et*  
92 *al.* 2020). ~~These experiments were e~~Conducted between 2010 and 2021, ~~by research projects~~  
93 ~~under the auspices of the Joint Fire Science Program (<http://www.firescience.gov>) and the~~  
94 ~~Department of Defense Strategic Environmental Research and Development Program (SERDP)~~  
95 ~~(<https://serdp-estep.org/>); these forest fire experiments covered~~ The burn plots for these  
96 ~~experiments, which were in the same areas of the New Jersey Pine Barrens, ranging~~ from  
97 ~~approximately about~~ 5 to 100 hectares, ~~in size, with forest understory vegetation (average about 1~~  
98 ~~m height) composed of blueberry, huckleberry and scrub oak and overstory vegetation (average~~  
99 ~~about 20 m height) composed of pitch pine and mixed oak.~~ Tturbulence data ~~were~~ collected  
100 using 3D sonic anemometers and thermocouples mounted on ~~a 20-m, a 10-m and a 3-m~~ 3-, 10-,  
101 20- and 30-m micrometeorological flux towers ~~within the burn plots~~. The data ~~from these NJ fire~~  
102 ~~experiments~~ revealed large-substantial variations in turbulence intensity, stress, and fluxes across  
103 the canopy layer, ~~which complicat~~inged the ~~evolution-understanding~~ of local turbulence regimes  
104 and their interaction with the spreading fires. ~~Specifically~~ Notably, ~~the data showed that~~ fire-  
105 induced increases in turbulent kinetic energy are considerably larger near the top of the forest  
106 canopy layer than within ~~it~~the canopy, ~~implying that~~suggesting a substantial vertical mixing or  
107 transport of fire emissions ~~(e.g., PM, moisture and heat) could be substantially larger~~ near the  
108 canopy top ~~than within the canopy layer~~ (Heilman *et al.*, 2015). The observations also ~~revealed~~  
109 ~~that~~ highlighted the persistence of an anisotropic turbulence regime ~~tends to persist~~ throughout  
110 the vertical extent of overstory canopy layers, even within ~~the~~ highly buoyant plumes s during the  
111 passage of fire fronts. The results suggested that spreading line fires ~~can have a substantial effect~~  
112 ~~on~~ could significantly affect the skewness of daytime velocity distributions typically found inside

113 forest vegetation layers, and ~~that~~ the contributions to turbulence production and evolution from  
114 mechanical shear production and diffusion ~~can be very~~could different markedly in the pre-fire  
115 and post-fire environments (Heilman *et al.*, 2017).

116 The data from both the TX grass fires and NJ forest understory fires have also provided  
117 insight into the turbulent momentum and heat transfer processes during ~~the~~ fires. ~~The fire-~~  
118 ~~e~~Enhanced turbulence updrafts and downdrafts during fires facilitate the transfer of warmer air  
119 (or lower momentum air) ~~from the surface~~ upward, ~~a process known as “ejection”~~ and colder air  
120 (or higher momentum air) downward, ~~to the surface, a process referred to~~ known as “ejection”  
121 and “sweep”, respectively ~~which act to redistribute energy or momentum between the combustion~~  
122 ~~layer and the atmosphere above~~ (Heilman *et al.*, 2021). ~~The a~~Analyses ~~of the data from the TX~~  
123 ~~and NJ fire experiments~~ suggested that wildland fires in grass or forest environments could  
124 substantially alter the relative importance of sweep and ejection processes in redistributing  
125 momentum, heat and other scalars in the lower atmosphere (Heilman *et al.*, 2021). ~~For turbulent~~  
126 ~~momentum transfer, s~~Sweep events ~~were found to play a~~ dominant momentum transfer role at  
127 the fire front, regardless of fire type, despite the stronger updrafts than downdrafts at the front.  
128 However, the effect of fires on turbulent heat transfer ~~is different~~ between ~~the~~ heading intense  
129 grass fires and backing low-intensity forest-understory fires. The former tended eds to be dominated  
130 by ejection events, while in the latter case ejection and sweep events are equally important  
131 (Heilman *et al.*, 2021).

132 ~~Both t~~The TX and NJ wildland fire experiments ~~mentioned above~~ were conducted over  
133 burn plots on relatively flat terrain. However, wildland fire behaviors can be affected  
134 significantly influenced by topography (Werth *et al.*, 2011; Sharples, 2009; Sharples *et al.*,  
135 2012). ~~This is because as~~ topography exerts a strong impactinfluence on both weather and fuel

136 conditions (Bennie *et al.*, 2008; Ebel, 2013; Billmire *et al.*, 2014; Calviño-Cancela *et al.*, 2017;  
137 Povak *et al.*, 2018). ~~In California, a~~ series of prescribed burn experiments ~~in California~~  
138 between 2008 and 2012 were conducted in complex terrain with burn plots on a simple slope  
139 (Seto and Clements *et al.*, 2011; Seto *et al.*, 2013; Clements and Seto, 2015; Amaya and  
140 Clements, 2020) or in a narrow valley (Seto and Clements, 2011). ~~The burn plots in these~~  
141 ~~experiments~~ ranged from 2 to 15 hectares in size, ~~but Although~~ all burn plots were dominated  
142 by grass fuels. ~~Data~~ from these experiments ~~collected using micrometeorological towers~~  
143 ~~augmented by other remote sensing equipment~~ provided unique information on the interactions  
144 between terrain-induced circulations and fire-induced flows. ~~The r~~Results ~~showed indicated~~ that  
145 terrain-induced slope flows and valley winds can interact with fire-induced flows, ~~to~~ enhance  
146 horizontal and vertical wind shears that subsequently contribute to turbulence production. ~~The~~  
147 Interactions of fire-induced flows with slope winds also produce local convergence or  
148 divergence with strong updrafts and downdrafts. Turbulence regimes tend to be anisotropic  
149 immediately above fire fronts, moving transitioning towards isotropic conditions higher up (Seto  
150 *et al.*, 2013, Clements and Seto, 2015; Amaya and Clements, 2020). ~~The d~~Data from these  
151 studies also revealed an increase in turbulent energy in both velocity and temperature spectra at  
152 higher frequencies, attributed to small eddies shed by as fire fronts ~~shed small eddies~~, and an  
153 increase at lower frequencies ~~that are~~ related to the strengths of the cross-stream wind component  
154 generated by the fire and enhanced by topography (Seto *et al.*, 2013).

155 The aforementioned field experiments were conducted on operational-scale (or  
156 management-scale) burn plots, ~~that ranged ranging~~ from several to 100 hectares, making and it  
157 ~~was not un~~feasible to cover such large burn plots with just a few micrometeorological towers.  
158 Consequently, the measurement strategy of these experiments was centered around tall towers



159 placed at couple of key spots in the burn plot to provide information on vertical variations of  
160 fire-atmosphere interactions. ~~However, T~~the lack of spatial coverage of the complex fuel and  
161 atmospheric conditions at these large burn sites makes interpretation of ~~the~~ limited observations  
162 challenging. Laboratory studies (e.g, Forthofer and Goodrick, 2011; Campbell-Lochrine *et al.*,  
163 2021; Di Cristina *et al.*, 2022) have the advantage of monitoring ~~the~~ fires using densely spaced  
164 instruments. ~~However~~Nevertheless, laboratory studies are often conducted under controlled  
165 conditions that may not necessarily be representative of the real fuel and atmospheric  
166 environments encountered in outdoor wildland fires. There exists an apparent gap in the  
167 observations of fire-atmosphere interactions between operational-scale burns and fine-scale  
168 laboratory experiments.

169 HereIn the context, we present analyses of turbulent data collected during a small-scale  
170 (10 m × 10 m) experimental burn, ~~in the field that~~ which was densely instrumented for the  
171 purpose of bridging the gap in our knowledge about fire-atmosphere interactions between  
172 operational-scale ( $\geq 10^3$  m<sup>2</sup>) and laboratory-scale ( $< 10^1$  m<sup>2</sup>) fire experiments. The primary  
173 question we aim to address is how a low-intensity surface fire may modify turbulence in the  
174 atmosphere just above the combustion zone. ~~More s~~Specifically, our analyses will explore ~~the~~  
175 ~~following~~ questions such as: How does the surface fire alter turbulence intensity and turbulent  
176 heat and momentum exchanges between the combustion zone and the atmosphere above?  
177 Whether and how would the fire change the partitioning of the heat and momentum fluxes into  
178 different types of events (both event number and event contribution)? How ~~does~~ the  
179 modifications of the fire on turbulence vary spatially across the burn plot? Answers to these  
180 questions could prove useful for predicting fire-atmosphere interactions, particularly the  
181 momentum and scalar exchanges between the fire and the atmosphere. Moreover, insights into

182 ~~spatial variability the answer to the last question~~ could ~~provide guidance regarding what the~~  
183 ~~determination of~~ horizontal grid spacing in coupled atmosphere-fire behavior models ~~is~~  
184 necessary to capture horizontal variability in near-surface atmospheric turbulence during the  
185 presence of surface fires.

186

## 187 **2 Method**

188

### 189 **2.1 Experiment and Instrumentation**

190 The experimental burn that this study focuses on took place on May 20, 2019 in a pitch  
191 and loblolly pine plantation at the Silas Little Experimental Forest in New Lisbon, New Jersey.  
192 This particularly burn was part of broader series of 35, densely instrumented, low-intensity  
193 surface fire experiments on 100 m<sup>2</sup> (10 m x 10 m) plots in this plantation conducted between  
194 March 2018 and June 2019 by a ~~SERDP~~ research project funded by the Department of Defense's  
195 Strategic Environmental Research and Development Program (SERDP). The overall goal of this  
196 research project was ~~that set out~~ to collect data using laboratory-scale (10<sup>0</sup>-10<sup>1</sup>m<sup>2</sup>) experiments,  
197 intermediate or fuel-bed-scale (10<sup>2</sup> m<sup>2</sup>) burns and management-scale (10<sup>3-4</sup> m<sup>2</sup>) prescribed fires  
198 to improve the understanding of combustion processes and fire-atmosphere interactions across  
199 scales (Gallagher *et al.*, 2022; Skwonski, *et al.*, 2021).

200 As shown in Figure 1, the 100 m<sup>2</sup> burn plot was densely monitored by instruments  
201 mounted on four parallel east-west-oriented trusses (A, B, C, D). On each truss, four 3D fast-  
202 response sonic anemometers (R.M. Young 81000V, Traverse City, MI, USA) were mounted at  
203 2.5 m above the ground level (AGL) to collect the east-west (*u*), north-south (*v*) and vertical (*w*)  
204 velocity components and temperature at a sampling rate of 10 Hz (Clark *et al.*, 2022a).

205 Additional 10-Hz temperature data were also obtained using fine-wire thermocouples (Omega  
206 SSRTC-GG-K-36, Omega Engineering, Inc., Stamford, CT, USA) mounted at a range of heights  
207 (0, 5, 10, 20, 30, 50, 100 cm) below the two inner trusses (B and C) (Clark *et al.*, 2022b). A  
208 radiometer/visible spectrum camera pair was mounted adjacent to each sonic anemometer to  
209 measure radiative heat fluxes and flame arrival times and persistence (Kremens *et al.*, 2022).  
210 Spatially explicit fire spread data were derived from infrared data collected by an infrared video-  
211 camera (A655SC, FOL6 100.0-650.0 C lens, FLIR Systems Inc., Wilsonville, OR, USA)  
212 mounted on top of a 10-m tower in the center of the plot (Skowronski *et al.*, 2022a). A custom  
213 field calorimetry hood (labeled TACO next to B2) with an inlet oriented over a portion of the  
214 fuel bed was used to sample O<sub>2</sub>, CO<sub>2</sub>, and CO concentrations in buoyant plumes (Campbell-  
215 Lochrie *et al.*, 2022). Gas concentrations were measured at 1 Hz using an Infrared gas analyzer  
216 (Crestline NDIR 7911, Crestline, Livermore, CA, USA).

217         The analyses here focused only on the data from the 4×4 sonic anemometer array. All  
218 sonic anemometer data underwent a quality assurance and control process to remove spurious  
219 values (Clark *et al.*, 2022a). Initially, data that were collected prior to a designated common start  
220 time was removed, providing a starting point for the observations for the burn period. Next, the  
221 data from sonic anemometers include a self-reporting diagnostic column where any non-zero  
222 number is considered an invalid measurement, so any measurement that reported a non-zero  
223 diagnostic code was removed. Following these initial steps, data that fell outside the sonic  
224 anemometer operating parameters (wind speed: ±40 m/s; temperature: ± 50 °C) were also  
225 removed.

226         The horizontal wind velocities were rotated into a streamwise coordinate system where  
227 the *u*-component (streamwise component) is aligned with the prevailing wind direction, and the

228  $v$ -component (cross-stream component) is perpendicular to the prevailing wind direction pointing  
229 to the left. Vertical winds were not corrected for tilt because of the short (<30 min) observational  
230 period and because the burn plot was on level ground and each sonic anemometer was carefully  
231 mounted and leveled so that the wind sensors were very close to true horizontal and vertical  
232 planes. The results (presented below) indeed suggested that the contamination of vertical  
233 velocity by horizontal velocities were negligibly small as the average vertical wind component  
234 during the pre-burn period was nearly zero.

235

## 236 **2.2 Fuel and ambient atmospheric conditions**

237 The primary fuel for this burn was pitch pine needles (*Pinus rigida* Mill.). Based on  
238 biometric and terrestrial laser scan measurements collected pre- and post-burn, the fuel mass was  
239 estimated to be about  $0.5 \text{ kg m}^{-2}$  and fuel moisture content about 5.5% (Skowronski *et al.*,  
240 2022b).

241 The ambient atmospheric conditions on the day of the burn is indicated using the data  
242 from a surface weather station located approximately 200 m northeast of the burn plot that has  
243 similar type of land cover as the burn plot (Figure 2). Ambient winds were very weak in the  
244 morning, varying in direction between south and west. Wind speeds increased in midday to about  
245  $5 \text{ m s}^{-1}$  along with a direction shift to southwest and west. This wind speed increase was likely  
246 due to the mixing of higher winds from above to the surface as the mixing layer grew higher  
247 during the day. The growth of the mixing layer was a result of increased turbulent mixing  
248 associated with surface heating, as indicated by an increase in surface temperatures from about  
249  $20 \text{ }^{\circ}\text{C}$  in the morning to slightly above  $30 \text{ }^{\circ}\text{C}$  around 1400 Local Standard Time (LST) and a

250 corresponding decrease in relative humidity from over 80% in the morning to less than 40% in  
251 the early afternoon.

252

### 253 **2.3 Fire spread**

254 The experiment started around 14:25 LST when a single 10-meter cotton cord was  
255 soaked in accelerant, ignited and then dropped on the fuel bed to produce a single, near linear  
256 ignition across the western border of the plot. Infrared imagery data (Figure 3) captured by the  
257 overhead infrared camera is used to evaluate the changes in temperature from just before ignition  
258 (Figure 3a), immediately after ignition (Figure 3b), and through the period following the ignition  
259 as the line fire spread with winds across the plot (Figure 3c-f). The average fire spread rate  
260 throughout the burn was ~~estimated~~evaluated from these data to be approximately  $5.4 \text{ cm s}^{-1}$ . The  
261 ignition produced a line fire parallel to the western boundary of the plot (Figure 3b). The line fire  
262 spread in the direction of the west-southwesterly background wind towards the east-northeast  
263 over the next few minutes (Figure 3c, d). The initial spread was faster on the northern portion of  
264 the domain, as expected from the south-southwesterly wind direction. As the fire burned through  
265 the northern portion of the plot, the fire front caught up in the southern portion (Figure 3e). The  
266 fire ended at around 14:32:16 LST as the fire front reached the eastern boundary of the plot and  
267 ran out of fuel to continue (Figure 3f).

268

### 269 **2.4 Data Analysis**

270 The quality-controlled 10-Hz wind and temperature data from the 3D sonic anemometers are  
271 used to calculate turbulent perturbations defined as the differences between the instantaneous  
272 observations and the mean values:

273 
$$\varphi' = \varphi - \bar{\varphi} \quad (1)$$

274 where  $\bar{\varphi}$  is the mean value that is estimated by block-averages

275 
$$\bar{\varphi} = \sum_{n=1}^N \varphi_n \quad (2)$$

277

278 Here,  $N$  is the number of samples over the averaging period or the time block and the mean  
279 values represent the mean state of the atmospheric flow. In traditional turbulence studies, mean  
280 state is usually determined by averaging the data over a period of a few minutes up to 1 hour,  
281 depending on atmospheric stability and the scale of interest. However, the block-averaged values  
282 during the period of active burning are likely to be contaminated by the fire and therefore poorly  
283 represent the mean background flow. To resolve this issue, Seto *et al.* (2013) and Heilman *et al.*  
284 (2015) proposed that the block-averaged means for the fire period be replaced by block-averaged  
285 means calculated during the pre-burn period. In order to adopt this approach, the observational  
286 period is divided into three periods representing pre-burn, burn and post-burn, which are  
287 described in detail below.

288 The arrival of the fire front at most locations in the sonic anemometer array was clearly  
289 marked by a sharp rise in temperature (Figure 4). However, the magnitudes of the temperature  
290 increase and the rates of increase vary with the location of the sonic anemometers because the  
291 shape of the flame front was irregular (Figure 3). Note that the sonic temperatures are limited to  
292 50 °C, which is the operational range for the instruments beyond which data are deemed  
293 unreliable. Based on the temperature time series and the time when the fire was ignited along the  
294 western boundary (14:25 LST), the 10-min period from 14:15:13 through 14:25:12 LST is  
295 defined as the pre-burn period over which the mean values for  $u$ ,  $v$ ,  $S$  (horizon wind speed),  $w$ ,  
296 and  $T$  are calculated, and these values are used for computing perturbations for the entire

307 experiment. The definition of the burn period, however, is complicated by the fact that the fire  
308 front reaches/leaves each sonic anemometer at a different time and consequently the true burn  
309 period across the plot varies somewhat depending on the location of each sonic anemometer.

300 To create a robust definition of the burn period that can be applied to all the sonic  
301 anemometers in the  $4 \times 4$  array, and eventually to other burns in the broader burn series, the  
302 sharp rise in sonic temperatures associated with fire front is measured using integer ( $n$ ) multiples  
303 of the standard deviation (denoted using  $\sigma$ ) of the average temperature over the pre-burn period.  
304 A threshold value that is too small (e.g., 1 or 2 times standard deviation) may not distinguish the  
305 increase in temperature associated with the fire front from normal temperature fluctuations  
306 during the day, but a value that is too large (e.g., 10 time standard deviation) may fail to detect  
307 the fire front associated with a small or moderate temperature increase. Figure 5 shows the  
308 number of sonic anemometers whose temperatures exceed  $n \times \sigma$  as  $n$  increases from 1 to 35, and  
309 the length of the exceedance period. As  $n$  increases from 1 to 8 or the threshold value for fire-  
310 induced temperature increase changes from  $1\sigma$  to  $8\sigma$ , the number of sonic anemometers drops  
311 from 16 to 13 and the period drops sharply from just under 60 min to about 6 min. Continued  
312 increases in the threshold values from  $8\sigma$  to  $25\sigma$  result in no change in the number of  
313 anemometers and very little change in the length of the period (less than 1 min). This analysis  
314 suggests that  $8\sigma$  ~~could~~ be used as the threshold for temperature increases associated with fire  
315 front. Thresholds lower than  $8\sigma$  would imply a burn period of 30- to 60-min long that, according  
316 to the time series in Figure 4, would include periods of no fire and therefore de-emphasize the  
317 effects of the fire in the resulting analyses. Applying this criterion to all the sonic anemometers  
318 and defining the burn period as between the first and last sonic temperature at or above the

319 threshold leads to the selection of the burn period as 14:26:13 to 14:32:29 LST. Finally, the 10  
320 min following the burn period (14:32:30 to 14:42:29 LST) is defined as the post-burn period.

321         Following the establishment of the three periods, wind and temperature perturbations are  
322 calculated using equations (1) and (2), where the pre-burn averaged values are used as means for  
323 the burn and post-burn periods. Strictly speaking, the perturbations calculated for the burn and  
324 post-burn periods are not classical turbulent perturbations; to differentiate the features from  
325 classical turbulence, they should be interpreted as being primarily fire-induced turbulent  
326 perturbations.

327         As noted above, horizontal wind velocity is rotated into a streamwise coordinate where  
328 the  $x$ -component (streamwise component,  $u$ ) is aligned with the prevailing wind direction and the  
329  $y$ -component (cross-stream component,  $v$ ) is perpendicular and pointing to the left of the  
330 prevailing wind. The prevailing wind direction for the rotation is determined by the 10-min pre-  
331 burn period average of wind directions across all 16 sonic anemometers. The average wind  
332 directions during the pre-burn period vary slightly across the 16 sonic anemometers, with mean  
333 and median wind directions of 225 and 226 degrees, respectively. The subtle variations in wind  
334 directions is possibly due to slight error in sensor alignment, rather than actual flow  
335 heterogeneity. The 226 degrees is used as the prevailing wind direction for the purpose of  
336 coordinate rotation.

337         The quality controlled, coordinate rotated data from the sonic anemometers are analyzed  
338 to determine fire-induced changes to turbulence intensity, vertical heat fluxes and vertical fluxes  
339 of horizontal momentum also known as shear stress just above the combustion zone by  
340 comparing values between the pre-burn and the burn periods. The values are also compared



341 between the pre-burn and post-burn periods to determine how quickly the effects of fire dissipate  
342 or how fast the atmosphere returns to the ambient state.

343 Turbulence intensity is measured by the turbulent kinetic energy (*TKE*) defined as the  
344 sum of the variance of the three velocity components:

$$345 \quad \quad \quad TKE = (\overline{u'^2} + \overline{v'^2} + \overline{w'^2}) / 2 \quad (3)$$

347  
348 Turbulent shear stress is commonly measured by shear velocity or friction velocity denoted by  
349  $u_*$  and the square of friction velocity is related to the magnitude of the kinematic vertical flux of  
350 horizontal momentum:

$$351 \quad \quad \quad u_*^2 = (\overline{u'w'^2} + \overline{v'w'^2})^{\frac{1}{2}} \quad (4)$$

352 where  $u'w'$  and  $v'w'$  are the vertical fluxes of streamwise and cross-stream momentum flux,  
353 respectively and the overbar denotes time average. The average period is 1 min for this analysis  
354 to be consistent with previous studies on fire-induced turbulence (Seto *et al.*, 2013; Heilman *et*  
355 *al.* 2021). Vertical kinematic heat flux is calculated as  $\overline{T'w'}$  and the averaging period is also 1  
356 min.

357 For the analyses of vertical turbulent fluxes of heat and horizontal momentum, a quadrant  
358 analysis technique (Katul *et al.*, 1997, 2006; Heilman *et al.*, 2021) is utilized to delineate the  
359 contributions to the turbulent heat or momentum transfer from four types of processes  
360 corresponding to the four quadrants of a  $w'$  (horizontal) and  $\varphi'$  (vertical) coordinate, where the  $w'$   
361 denotes vertical velocity perturbation and  $\varphi'$  denotes perturbations of temperature ( $T'$ ) or  
362 horizontal wind speed ( $S'$ ) in heat or momentum flux calculations, respectively. The four  
363 quadrants are: Q1:  $\varphi'w' > 0, \varphi' > 0, w' > 0$ ; Q2:  $\varphi'w' < 0, \varphi' > 0, w' < 0$ ; Q3:  $\varphi'w' > 0, \varphi' <$

364 0,  $w' < 0$ ; Q4:  $\varphi'w' < 0$ ,  $\varphi' < 0$ ,  $w' > 0$ . Note that the perturbation in horizontal wind speed  
365 ( $S'$ ), rather than the streamwise or cross-wind components ( $u'$  or  $v'$ ), are used for computing  
366 momentum flux following Heilman *et al.*, (2021):

$$367 \quad S' = S - \bar{S} \quad (5)$$

$$368 \quad S = \sqrt{u^2 + v^2} \quad (6)$$

369 The quadrant analysis is also known as sweep-ejection analysis (Heilman *et al.*, 2021)  
370 which associates each quadrant with a specific type of vertical turbulent transfer events. The  
371 names of the events and the associated quadrant designations, which are different for turbulent  
372 heat and momentum fluxes, are given in Table 1.

373 Based on the definition in Table1, ejection (Q1) and sweep (Q3) events contribute to  
374 positive vertical turbulent heat flux through the upward transfer of warmer air from below  
375 (ejection) or the downward transfer of cooler air from above (sweep), while inward interaction  
376 (Q2) and outward interaction (Q4) events contribute to negative turbulent heat flux through the  
377 downward transfer of warmer air from above (inward interaction) or the upward transfer of  
378 cooler air from below (outward interaction). For vertical flux of horizontal momentum, inward  
379 interaction and outward interaction events contribute to positive flux through the upward transfer  
380 of faster moving air (outward interaction) or the downward transfer of slower moving air (inward  
381 interaction), while sweep and ejection events contribute to negative momentum flux through the  
382 downward transfer of faster moving air (sweep) or the upward transfer of slower moving air  
383 (ejection). Note that the warmer/cooler or faster/slower air is relative to the air in the adjacent  
384 layers.

385 The sweep-ejection analysis calculates the proportion of a given type of events by simply  
386 counting the number of events or the data points in the 10 Hz time series that fall within the  
387 given quadrant. The contributions of the given type of events to the average turbulent fluxes over  
388 a given time period ( $T_p$ ) are calculated, following Heilman *et al.* (2021), by the integral

389

$$390 \quad \overline{\varphi'w'}_Q = \frac{1}{T_p} \int_0^{T_p} \varphi'(\tau)w'(\tau)\varepsilon_Q d\tau \quad (7)$$

391

392 where  $\varepsilon_Q$  is 1 for the given quadrant and zero otherwise,  $\tau$  is time and  $\varphi'$  is temperature or  
393 horizontal wind speed perturbation for heat or momentum fluxes, respectively.

394

### 395 **3 Results and Discussion**

396

#### 397 **3.1 Fire-Induced Perturbations to Wind and Temperature**

398 Before we examine fire-induced changes to turbulence in ambient atmosphere, we first  
399 take a look at the response of the instantaneous temperature and wind to the surface line fire  
400 recorded by the 16 sonic anemometers as the fire spread from west to east across the 10 m ×10 m  
401 burn plot (Figure 6). Note that perturbation temperatures ( $T'$ , see Eq. 1), instead of actual  
402 temperatures, are shown to accommodate the magnitude difference between temperature and  
403 wind, ~~and therefore making it easier to visualize~~ facilitating a more coherent visualization of the  
404 ~~jointly the~~ effects of the fire on temperature and wind.

405 The natural or non-fire fluctuation recorded during the pre-burn period are small, with  
406 magnitudes generally less than 2.5 m s<sup>-1</sup> for  $u$ , 1 m s<sup>-1</sup> for  $v$  and 2.5 °C for  $T'$ . The fire impinging  
407 upon the sonic anemometers is marked by a sharp increase in  $T'$ , but the magnitude of the

408 temperature changes depend heavily on location, from very little change on the western side (A1,  
409 B1, C1, D1) of the burn plot where the fire was ignited, to a nearly 20°C increase on the eastern  
410 side (A4, B4, C4, D4). This spatial heterogeneity in  $T$  is consistent with the pattern of the fire  
411 spread from the western boundary toward the east and northeast by the southwesterly ambient  
412 wind (Figure 4). During the burn period, the  $u$  fluctuations decreased slightly while the  $v$   
413 fluctuations increased. The  $v$ -component no longer fluctuated around zero, as in the pre-burn  
414 period, but rather it was dominated by negative values, indicating a systematic shift in wind  
415 direction. There was a tendency for  $u$  and  $T$  to return towards the pre-burn conditions after the  
416 burn, but the  $v$  component remained negative during the post-burn period.

417         The observed changes in the distribution of wind and temperature values associated with  
418 the fire at all 16 sonics are summarized by the box-whisker plots in Figure 7. The pre-burn mean  
419 is 1.7 m s<sup>-1</sup> for the streamwise wind component  $u$  and near zero (-0.04 m s<sup>-1</sup>) for the cross-stream  
420 component  $v$ . The pre-burn vertical velocity distribution also has near zero mean, which  
421 confirms that the sonic anemometers were well-leveled. During the burn period, the mean of  $u$   
422 dropped in magnitude from 1.7 to 1.05 m s<sup>-1</sup> while the mean of  $v$  increased in magnitude from -  
423 0.04 to -0.65 m s<sup>-1</sup>, indicating an overall shift in wind direction from southwesterly to west-  
424 southwesterly. This change in the horizontal wind components suggests that ambient air was  
425 drawn towards the fire producing convergence at the fire front. There is also a fire-induced  
426 widening of the distributions of the horizontal wind components, particularly the  $v$  component,  
427 and an increase in the number of outliers with magnitudes that nearly doubled the pre-fire  
428 magnitude. The large negative values in  $v$  during the burn period reinforce the suggestion of  
429 convergence in the vicinity of the fire.

430 Interestingly, there is little evident change in the overall distribution of  $w$  during the burn  
431 period, except that more and larger outliers are indicated. The maximum updrafts (downdrafts)  
432 during the burn period reach speeds of nearly  $6 \text{ m s}^{-1}$  ( $-5 \text{ m s}^{-1}$ ), which is more than double those  
433 of the pre- and post-burn periods, suggesting that intermittent turbulent eddies associated with  
434 the fire could have a strong impact on vertical velocity just above fuel bed. The  $T'$  distribution  
435 also widens substantially during the burn period ( $\sigma=4.24 \text{ }^\circ\text{C}$ ) compared to the pre-burn period  
436 ( $\sigma=0.48 \text{ }^\circ\text{C}$ ), with the maximum temperature perturbation reaching nearly  $20^\circ\text{C}$ .

437 The influence of the fire on the horizontal wind components continues into the post-burn  
438 period, as the post-burn distributions of  $u$  and  $v$  fall between those of the pre-burn and burn  
439 periods. In contrast, the post-burn  $w$  distribution returns to a distribution very close to that of the  
440 pre-burn period. Similarly, the  $T'$  distribution during the post-burn period is very similar to that  
441 of the pre-burn period. The similarities between the  $w'$  and  $T'$  distributions suggest that the two  
442 variables are closely related to each other, with large updrafts during the burn period being  
443 generated primarily by heating. This result suggests that the fire-induced circulation exhibits  
444 behavior more consistent with a buoyant plume than mechanically forced rising motion resulting  
445 from converging surface air.

446

### 447 **3.2 Intensity of Fire-Induced Turbulence**

448 We now explore the modifications of the fire to atmospheric turbulence properties just  
449 above the combustion zone. The first question to address is how turbulence intensity quantified  
450 by  $TKE$  in Eq. (3) is modified by the fire and how the modification may vary with location in the  
451 burn plot. Figure 8 shows time series of 1-minute averaged  $TKE$  and its three components (the  
452 variance of the three velocity components) for each of the sonic anemometers. The time series

453 indicate lower *TKE* values in the pre-burn period, larger values during the burn period, and  
454 values remaining high in the post-burn period. The burn period *TKE* is primarily driven by an  
455 increase in horizontal velocity variance,  $\overline{u'^2}$  and  $\overline{v'^2}$ , particularly the cross-stream component  
456  $\overline{v'^2}$ . The *TKE* values remain high into the post-burn period and, at several sonic anemometers  
457 (D3 and C4), the post-burn *TKE* peaks are comparable with or higher than the peaks observed  
458 during the burn period.

459         The box-whisker plots in Figure 9 depict the fire-induced changes to the distribution of  
460 turbulence intensity as observed by all 16 sonic anemometers. Averaging across all the  
461 instruments, the burn period mean *TKE* is  $1.25 \text{ m}^2\text{s}^{-2}$ , which is roughly double the pre-burn mean  
462 of  $0.697 \text{ m}^2\text{s}^{-2}$ . The interquartile range of the burn period *TKE* is nearly three times the pre-burn  
463 period range. Despite the increase in the mean and the interquartile range of the *TKE* from the  
464 pre-burn to the burn period, the mean *TKE* values are still below  $3 \text{ m}^2\text{s}^{-2}$ , which is a threshold  
465 sometimes used as an indicator for substantial boundary-layer turbulence (Stull, 1988; Heilman  
466 and Bian, 2013), suggesting that this low-intensity surface line fire fails to produce a  
467 substantially turbulent environment at the levels just above the fuel bed. The mean *TKE* in the  
468 post-burn period does not return to that of the pre-burn period and remains elevated ( $1.21 \text{ m}^2\text{s}^{-2}$ ).  
469 While the  $\overline{w'^2}$  returns to the pre-burn conditions, the horizontal components remain elevated.

470         More specifically,  $\overline{u'^2}$  and  $\overline{v'^2}$  make up 53.0% and 38.5% of the average pre-burn *TKE*,  
471 respectively. During the burn period, the contribution to *TKE* from  $\overline{u'^2}$  decreases slightly to  
472 49.1% and the contribution from  $\overline{v'^2}$  increases substantially to 43.3%. As noted earlier (Figures 6  
473 and 7), the burn period also exhibits a larger range of horizontal and vertical wind components,  
474 which is consistent with the larger range of *TKE* values in Figure 9.

475 In the post-burn period, the distribution of vertical velocity variance returns to the pre-  
476 burn distribution. However, the range of values in the horizontal components are smaller during  
477 the post-burn period than the burn period, but still larger than during the pre-burn period. The  
478 medians of the horizontal *TKE* components are higher in the post-burn period than in either of  
479 the other periods. While the  $\overline{u'^2}$  outliers (above the 99.3rd percentile) decrease, the  $\overline{v'^2}$  outliers  
480 increase in magnitude. As was previously discussed, post-burn average wind directions differ  
481 slightly from the pre-burn, accompanied by increases in the magnitude of the horizontal winds  
482 (Figures 6 and 7). This result is consistent with elevated *TKE* values persisting into the period  
483 after the end of the fire.

484 Additional analysis of the variance of the three velocity components enables an  
485 assessment of turbulence anisotropy indicated by the ratio of  $\overline{w'^2}$  to  $2xTKE$ . When this ratio  
486 approaches 1/3 for a given time period, the period can be said to experience an isotropic  
487 turbulent regime (Heilman *et al.*, 2015). The mean  $\overline{w'^2}$  for all the sonic anemometers is 0.0597  
488  $m^2s^{-2}$  for the pre-burn period, 0.0931  $m^2s^{-2}$  for the burn period, and 0.052  $m^2s^{-2}$  for the post-burn  
489 period, which yields an anisotropy ratio of 0.042, 0.036, 0.021 for the pre-burn, burn and post-  
490 burn periods, respectively. As the anisotropy ratios are well below 1/3 in all three periods, the  
491 turbulence regime just above the combustion zone remains anisotropic at all time. It is worth  
492 noting that in contrary to the belief that the increase in vertical velocity variance in response to  
493 the surface heating during the burn should act to move turbulence towards a more isotropic  
494 regime, the ratio here is slightly smaller during the burn period than the pre burn period largely  
495 because the fire-induced increase in the cross-stream velocity variance is larger than the increase  
496 in the vertical velocity variance. Heilman and Bian (2015) calculated the anisotropy ratios at 3  
497 m above ground for two forest understory fires. The ratio decreased from 0.118 to 0.0718 from

498 pre-burn to burn in one experiment, but increased from 0.089 pre-burn to 0.13 in another  
499 experiment. Since the sonic anemometers located on the western and southern sides of the burn  
500 plot show no clear increase in  $\overline{w'^2}$ , the anisotropy ratio is also calculated for each sonic to verify  
501 that the mean values did not mask anisotropy variations at individual locations in the burn plot.  
502 No individual sonic anemometer reaches a ratio of 1/3, and the highest individual ratio (0.133) is  
503 found at sonic anemometer A4 during the burn period. This result indicates that overall, the *TKE*  
504 just above the combustion zone is highly anisotropic and is dominated by the horizontal  
505 components for this burn. This result is not surprising as the sonic anemometers are located only  
506 2.5 m above ground where horizontal turbulence would be expected to dominate over vertical  
507 turbulence (Heilman *et al.*, 2015).

508

### 509 **3.3 Fire-Induced Shear Stress**

510 To address the question on how the surface fire alter turbulent momentum transfer  
511 between the combustion zone and the atmosphere above, we next explore fire-induced changes  
512 to turbulent momentum fluxes or shear stress measured by friction velocity described in Eq. (4).  
513 Figure 10 shows time series of 1-minute averaged  $u_*^2$  and the streamwise  $\overline{u'w'}$  and cross-  
514 stream  $\overline{v'w'}$  stress components (the momentum flux), measured by each of the sonic  
515 anemometers for the three periods. Kinematic momentum fluxes and  $u_*^2$  are similar across all  
516 the sonic anemometers during the pre-burn period, although three of the northernmost  
517 instruments (A2, A3, and A4) indicate a negative spike in  $\overline{u'w'}$  just before the start of the burn  
518 period. These spikes contribute to an increase in  $u_*^2$  at this time as well. It is ~~not~~unclear what  
519 caused these features, but candidates include an anomalous burst of wind along the northern edge



520 of the burn plot and possible contamination of the wind data by activities of the burn managers  
521 as they prepared to ignite the fire.

522 During the burn period, the values of  $\overline{u'w'}$  and  $\overline{v'w'}$  increase somewhat, leading to  
523 increases in the  $u_*^2$  values. The fire-induced changes generally increase in magnitude from west  
524 (left) to east (right) and south to north, consistent with the fire-spread pattern. The largest  
525 increase occur at the easternmost (right) locations, particularly A4 and C4 where  $u_*^2$  values  
526 nearly doubled. The smallest increases are not found at the westernmost locations, but at C2 and  
527 D2. With a few exceptions,  $\overline{u'w'}$  and  $\overline{v'w'}$  are negative in the beginning of the burn period,  
528 turning positive later in the period. The  $\overline{u'w'}$  values exhibit the largest burn period variation at  
529 A4, followed by B4, and similar patterns are observed for  $\overline{v'w'}$ . Overall, variations in  $u_*^2$  suggest  
530 an increase in shear stress magnitude in the burn period compared to the pre-burn period, with  
531 the easternmost sonic anemometers recording 1-minute averaged values that are far greater than  
532 the westernmost sonic anemometers.

533 During the post-burn period, some sonic anemometers (A2, B2, C1, C2, D2) recorded  
534 higher  $u_*^2$  than during the burn period, while others (A1, B1, B3, C2, C3, D3) recorded values  
535 similar to the burn period. In either case, the average values are larger than during the pre-burn  
536 period. The maximum post-burn values among all the sonic anemometers occur at A2 for  $u_*^2$   
537 and  $\overline{v'w'}$  and C1 for  $\overline{u'w'}$ , both of which are larger than their burn-period peaks.

538 The overall distributions of  $u_*^2$ ,  $\overline{u'w'}$ , and  $\overline{v'w'}$  from all 16 sonic anemometers are  
539 depicted in Figure 11. During the pre-burn period,  $\overline{u'w'}$  is negative, with a mean value of -0.015  
540  $\text{m}^2 \text{s}^{-2}$ , indicating an overall downward transfer of higher streamwise momentum air, which is  
541 expected as wind speed usually increases with height. The mean of the cross-stream momentum

542 flux  $\overline{v'w'}$  is near zero ( $0.007 \text{ m}^2 \text{ s}^{-2}$ ). However, the spread of the two components is similar, with  
543 standard deviations of  $0.057 \text{ m}^2 \text{ s}^{-2}$  and  $0.046 \text{ m}^2 \text{ s}^{-2}$  for  $\overline{u'w'}$  and  $\overline{v'w'}$ , respectively. The pre-burn  
544 stress  $u_*^2$  of  $0.061 \text{ m}^2 \text{ s}^{-2}$  ( $u_* = 0.25 \text{ m}^2 \text{ s}^{-2}$ ) is typical for daytime surface layers.

545 An increase in the downward (upward) transfer of higher streamwise (cross-stream)  
546 momentum is observed during the burn period as the median values become more negative for  
547  $\overline{u'w'}$  and more positive for  $\overline{v'w'}$ . However, the mean values change little from the pre-burn  
548 period. The spread is doubled from a standard deviation of  $0.046$  to  $0.098 \text{ m}^2 \text{ s}^{-2}$  for  $\overline{u'w'}$  and  
549 nearly tripled from  $0.05$  to  $0.124 \text{ m}^2 \text{ s}^{-2}$  for  $\overline{v'w'}$ . The stronger upward transfer of cross-stream  
550 momentum is consistent with the generation of cross-stream wind and updrafts in the vicinity of  
551 the surface fire. Despite this overall fire-induced increase in  $\overline{v'w'}$ , the distribution of the cross-  
552 stream momentum is negatively skewed by large negative outliers, suggesting occasional transfer  
553 of higher cross-stream momentum by downdrafts near the vicinity of the fire. Both the mean and  
554 standard deviation of  $u_*^2$  values are doubled to  $0.13 \text{ m}^2 \text{ s}^{-2}$  and  $0.086 \text{ m}^2 \text{ s}^{-2}$ , respectively, over the  
555 pre-burn values. The peak 1-min averaged values of  $u_*^2$  exceed  $0.4 \text{ m}^2 \text{ s}^{-2}$  (or a friction velocity  
556 of  $0.6 \text{ m s}^{-1}$ ), which is 2.5 times larger than the pre-burn values. Clements *et al.* (2008) also  
557 observed a three-fold increase in friction velocity in their experiment involving a high intensity  
558 grass fire, although the absolute values of the friction velocity in their experiment were five  
559 times larger ( $1$  and  $3 \text{ m s}^{-1}$  before and during the fire) than the current experiment.

560 The mean post-burn  $u_*^2$  value ( $0.10 \text{ m}^2 \text{ s}^{-2}$ ) is lower than that of the burn period but still  
561 higher than the pre-burn value, driven primarily by the cross-stream component. The values of  
562 the  $\overline{v'w'}$  ( $0.0471 \text{ m}^2 \text{ s}^{-2}$ ) in the post-burn period is more than six times the pre-burn average  
563 ( $0.0072 \text{ m}^2 \text{ s}^{-2}$ ), with a standard deviation ( $0.069 \text{ m}^2 \text{ s}^{-2}$ ) that is between the pre-burn period

564 (0.046) and burn period (0.096) values. The mean friction velocity therefore does not return to  
565 the pre-burn average, although it is lower than the average during the burn period. Other  
566 experiments (e.g. Clements *et al.*, 2008; Heilman, *et al.* 2019) noted a return of friction velocity  
567 to pre-burn values soon after the passage of the fire front, during a period when smoldering was  
568 occurring. The results of this analysis suggest that friction velocities do not quickly return to pre-  
569 burn values on all fires.

570

### 571 **3.4 Fire-Induced Turbulent Heat Flux**

572 We proceed to examine the impact of the fire on turbulent heat flux. Time series of 1-  
573 minute average kinematic turbulence sensible heat flux  $\overline{T'w'}$  for each sonic anemometer are  
574 shown in Figure 12 for the three periods, which also shows the overall distribution of heat fluxes  
575 for all the sonic anemometers. In the pre-burn period, the sonic anemometers recorded  
576 background  $\overline{T'w'}$  values that averaged around  $5.25 \times 10^{-2} \text{ }^\circ\text{C m s}^{-1}$  (or  $52.7 \text{ W m}^{-2}$  after multiplying  
577 by the density and heat capacity of air), with a standard deviation of  $3.41 \times 10^{-2} \text{ }^\circ\text{C m s}^{-1}$  ( $34 \text{ W m}^{-2}$ ).  
578 During the burn period, a fire-induced increase in  $\overline{T'w'}$  is evident at all but the westernmost  
579 sonic anemometers (A1, B1, C1, and D1), with larger increases appearing at the easternmost  
580 locations. The largest  $\overline{T'w'}$  values generally occur early in the burn period, with the A4 sonic  
581 having the largest  $\overline{T'w'}$  value of  $2.13 \text{ }^\circ\text{C m s}^{-1}$  ( $2.138 \text{ kW m}^{-2}$ ). Based on the IR imaging (Figure  
582 4), after the first three minutes of the burn period there is a slight shift in the burn direction  
583 towards the southeastern side of the plot. This shift in direction is apparent in the time series for  
584 the D4 sonic anemometer, which is located on the southeastern corner of the burn plot, where  
585 elevated  $\overline{T'w'}$  values are recorded late in the burn period, at a time when the values have

586 dropped at most of the other sonic anemometers. The overall distribution of the burn-period  $\overline{T'w'}$   
587 is skewed by larger values since the plot mean was  $0.268 \text{ K m s}^{-1}$  ( $269 \text{ W m}^{-2}$ ) but the median  
588 was just  $0.0974 \text{ }^\circ\text{C m s}^{-1}$  ( $98 \text{ W m}^{-2}$ ).

589 Values of  $\overline{T'w'}$  during the post-burn period quickly drop back to just slightly above the  
590 pre-burn values, with a mean of  $6.35 \times 10^{-2} \text{ }^\circ\text{C m s}^{-1}$  ( $64 \text{ W m}^{-2}$ ) and a standard deviation of  
591  $3.76 \times 10^{-2} \text{ }^\circ\text{C m s}^{-1}$  ( $38 \text{ W m}^{-2}$ ). However, the post-burn period contains several outliers (above the  
592 99.3% percentile), indicating the influence of smoldering on some of the sonic anemometers  
593 even after the fire has exited the burn plot. A specific example of the smoldering effect is the D4  
594 sonic anemometer, where the post-burn  $\overline{T'w'}$  ( $0.126 \text{ }^\circ\text{C m s}^{-1}$  or  $126 \text{ W m}^{-2}$ ) is about twice the  
595 pre-burn value. The overall modest increase of  $\overline{T'w'}$  in the post-burn period compared to the pre-  
596 burn period was also observed in the two wildland fire experiments described in Heilman *et al.*  
597 (2019).

598

### 599 **3.5 Quadrant Analyses**

#### 600 **3.5.1 Turbulent heat fluxes**

601 The analysis above provided a quantitative assessment of fire-induced changes to the  
602 turbulent heat and momentum fluxes through comparisons of flux values between the pre-burn  
603 and the burn periods. However, such analysis cannot reveal what types of heat or momentum  
604 transfer events are mostly affected by the fire. We apply the quadrant analysis method (also  
605 known as sweep-ejection analysis) described earlier (Table 1) to the observed turbulent fluxes to  
606 provide additional insight into how the fire changes the composition of heat and momentum  
607 fluxes. By partitioning the total heat and momentum fluxes into four quadrants representing

608 different types of flux events, the quadrant or sweep-ejection analysis allows for the delineation  
609 of the fire influence on specific types of turbulent heat and momentum transfer processes.

610         Figure 13 shows the relative contributions and the proportional number of occurrence of  
611 the different heat-flux events (i.e., sweeps, ejections, outward interactions and inward  
612 interactions) during each period, observed by each of the 16 sonic anemometers. During the pre-  
613 burn period, the partitioning among the four types of events (see Table 1) by contribution and  
614 proportion exhibits little variation across the 16 sonic anemometers. At all locations, the ejection  
615 and sweep dominate, accounting for over 60% of the total events, with sweep being slightly  
616 larger. The rest is split between outward interaction and inward interaction events, with the  
617 former slightly outnumbering (20-23%) the latter (14-19%). A similar partitioning is observed  
618 for the event contributions for the heat fluxes, but the ejection events, despite being slightly less  
619 frequent, contribute more to the heat flux than do the sweep events. This apparent inconsistency  
620 between the partitioning of the event number and the event contribution suggests that ejection  
621 events likely involve larger eddies and stronger heat transfer compared to sweep events. This  
622 pre-burn period partitioning is similar to previous ambient daytime measurements observed in  
623 other studies (e.g., Heilman *et al.*, 2021).

624         The burn period is marked by substantial heterogeneity across the 16 sonic anemometers.  
625 Despite differences in the magnitudes of contributions to the heat fluxes amongst the sonic  
626 anemometers, the increases in the overall positive mean heat flux during the burn period can be  
627 largely attributed to increases of ejection events that contribute to positive heat fluxes through  
628 upward transfer of warmer air from the combustion zone to the atmosphere above. There is also  
629 an increase in the negative contribution from inward interaction events, which represents the  
630 downward transfer of warmer air from the atmosphere to the combustion zone. The contributions

631 to the overall mean heat flux by the other two types of events, sweep and outward interaction,  
632 show little change from the pre-burn to the burn periods, which suggests that the turbulent heat  
633 transfer processes represented by these types of events, namely downward transfer of colder air  
634 from above to the surface or upward transfer of colder air from the combustion zone to the  
635 atmosphere, are not very sensitive to the presence of a low-intensity fuel-bed-scale surface fire.

636         Compared to the partitioning in event contribution, the fire-induced changes to the  
637 partitioning in event number are less clear. In general, the sonic anemometers that show an  
638 increase in the contribution by inward interaction events also exhibit an increase in the number  
639 of inward interaction events from the pre-burn to the burn periods. However, an increased  
640 contribution to the overall mean heat flux by ejection events does not correspond to an increase  
641 in the number of the ejection events. The increased number of sweep events are in agreement  
642 with the increased sweep contributions at several sonics (A2-A4 and B2-B4), although the sweep  
643 contributions are overwhelmed by that of the ejection contributions at these sonic anemometers.

644         A key finding from this heat flux sweep-ejection analysis is that turbulent heat fluxes  
645 during the burn period are overwhelmingly dominated by ejection events, but there is usually a  
646 small or no increase in the number of ejection events. This suggests that the presence of a low-  
647 intensity fuel-bed-scale fire does not necessarily produce more upward turbulent heat transfer  
648 events, but instead, it produces stronger events that quickly transfer and diffuse the sensible heat  
649 generated by combustion into the ambient atmosphere above.

650         During the post-burn period, most sonic anemometers show vertical heat flux values that  
651 are smaller than the burn period but still larger than the pre-burn period. The largest contribution  
652 to the overall mean heat flux is usually from sweep events, accompanied also by an increase in  
653 the number of the events, indicating the occurrence of many events where cold air is transferred

654 downward. The post-burn period also exhibits an increase in the heat-flux contributions from  
655 outward interaction events, which represent downward transfer of warm air. Similar to the burn  
656 period, inward interaction events, both in contribution and number, vary considerably across the  
657 sonic array.

658 Figure 14 shows the partitioning of both the event number and the event contribution to  
659 turbulent heat fluxes using data from all 16 sonic anemometers, which highlights more clearly  
660 how the fire modifies the overall heat flux regime. Similar to the heat flux quadrant analysis for  
661 individual sonic anemometers, the heat flux events averaged across the sonic anemometer array  
662 for the pre-burn period is dominated by sweep (32%) and ejection (28%) events. Inward  
663 interaction events occur with the least proportion (17%), followed by outward interaction events  
664 (23%). The sweep and ejection events, which contribute to positive heat fluxes, are much larger  
665 in magnitude than the negative heat flux contributions from the inward and outward interaction  
666 events. The dominance of sweep and ejection events for the turbulent heat fluxes during the pre-  
667 burn period follows observations made in previous studies (Heilman *et al.*, 2021).

668 The combined proportions of sweep and ejection events (both contributing to positive  
669 heat fluxes) and the outward and inward interaction events (both contributing to negative heat  
670 fluxes) remain similar between the burn and the pre-burn period. However, between the two  
671 types of events in each group, one (sweep, inward interaction) increases and the other (ejection,  
672 outward interaction) decreases in proportion. Previous fire experiments also reported an increase  
673 in sweep events and a generally proportional decrease in ejection events (Heilman *et al.*, 2021),  
674 but the magnitudes of the changes are larger than what is observed here, likely because the  
675 previous fires are more intense. Additionally, modest changes in the partitioning of the event  
676 number and contributions for this fire could be a byproduct of combining data from sonic

677 anemometers that are not strongly affected by the fire front (i.e. the westernmost sonic  
678 anemometers) with those that experience more substantial changes.

679           The large changes in the contributions of the heat flux events during the burn period  
680 suggest that this fire has greater impacts on the event contributions to the mean turbulent heat  
681 fluxes than on the event number. Specifically, ejection event contributions dominate in the burn  
682 period, making up 70.4% of the total contribution, while sweep and outward interaction  
683 contributions decrease by a third and a sixth, respectively, compared to their contributions during  
684 the pre-burn period. The magnitude of the contribution from inward interaction events increases  
685 slightly but is quite similar to the contribution during the pre-burn period.

686           Heat flux events in the post-burn period more closely resemble the pre-burn period than  
687 the burn period, but the event contributions and the event number do not return entirely to their  
688 pre-burn values. As noted in the analyses of *TKE* and kinematic heat flux (Figures 9 and 11), this  
689 result is consistent with smoldering occurring in the burn plot during the post-burn period. The  
690 sweep event contribution during the post-burn period is 1.5 times higher than during the pre-burn  
691 period and 1.3 times higher than during the burn period. Compared to the pre-burn values, the  
692 post-burn period event contributions are slightly higher for outward interaction events and  
693 slightly lower for ejection and inward interaction events. Overall, the post-burn period is  
694 dominated by contributions from sweep events (37.7%), which is followed by ejection event  
695 (25.3%) although lower than pre-burn values. These results differ somewhat from the Heilman *et*  
696 *al.* (2021) in that they reported both sweep and ejection events returning to pre-burn values,  
697 while only ejection events return to pre-burn values for this fire.

698



### 699 3.5.2 Turbulent momentum fluxes

700           Quadrant analysis is also applied to partition the vertical turbulent kinematic flux of  
701 horizontal momentum  $\overline{S'w'}$  into four different types and the results for each of the 16 sonic  
702 anemometers are shown in Figure 15. During the pre-burn period, the overall mean momentum  
703 fluxes are negative at all but two sonic anemometers (C1, C2) where the flux is slightly positive.  
704 Between the two types of events that contribute to negative momentum fluxes, the sweep events  
705 (downward transfer of higher horizontal momentum air from the atmosphere to the combustion  
706 zone) contribute more than the ejection events (upward transfer of lower horizontal momentum  
707 air from the combustion zone to the atmosphere above), which is consistent with the slightly  
708 higher number of sweep events than ejection events. Between the two types of events that  
709 contribute to positive momentum fluxes, the outward interaction events (upward transfer of  
710 higher horizontal momentum air from the combustion zone to the atmosphere above) contribute  
711 more than the inward interaction events (downward transfer of lower horizontal momentum air  
712 from the atmosphere to the combustion zone), although the number of the inward and outward  
713 interaction events is similar .

714           The changes from the pre-burn period to the burn period vary substantially by location,  
715 but the sign of the overall mean momentum fluxes remains unchanged at most locations. The  
716 most pronounced and consistent change across the anemometer array is a substantial increase in  
717 the proportional number of inward interaction events and, to a lesser degree, the contribution  
718 from these events. The ejection events also exhibit an increase in the number and the  
719 contribution at most of the sonic anemometer locations. There is a general decrease in the  
720 number of sweep and outward interaction events, but the contributions are not consistent, with  
721 some sonic anemometers showing an increase while others experience a decrease in contribution.

722 An exception to the above general observations between the pre-burn and burn periods is  
723 B4, where the overall momentum flux shifts from negative to positive due to an increase in  
724 outward interaction contribution by as much as 5 times the pre-burn magnitude. The amount of  
725 increase in the contribution from the outward interaction events, however, does not match the  
726 small increase (approximately 10%) in the event number, which suggests that the increase in the  
727 overall momentum flux magnitude at this location is likely due a small number of extremely  
728 strong events of upward transfer of higher horizontal momentum air associated with large,  
729 energetic eddies generated by the surface fire.

730 The large heterogeneity in the event contribution values for the momentum fluxes across  
731 the sonic anemometer array during the burn period dissipated substantially into the post-burn  
732 period. The event contribution and event number distributions once again become less dependent  
733 on the locations of the sonic anemometers. Despite this tendency to return to the pre-burn  
734 distribution, the post-burn period experiences larger contributions from, and higher number of  
735 ejection and inward interaction events than sweep and outward interaction events, which is  
736 opposite to the pre-burn period and similar to the burn period.

737 Figure 16 shows a quadrant analysis that combines data from all the sonic anemometers,  
738 which allows for an assessment of how the fire modified the momentum flux turbulence regime  
739 for the entire burn plot. Overall, sweep (31.9%) and outward interaction (26.6%) events  
740 dominate the momentum flux contributions in the pre-burn period. The increases in the  
741 proportion of inward interaction and ejection events from the pre-burn to the burn periods make  
742 the contributions more balanced across the four quadrants, suggesting that the different event  
743 contributions are more similar to each other during the burn than the pre-burn period. In the post-  
744 fire period, inward interaction events contribute more to the mean momentum flux (25.7%) than

745 during the pre-fire period (18.1%). The event number distributions in the combined analysis  
746 echoes the results from the individual sonic anemometers, with the pre-burn period showing  
747 similar values for all four quadrants, a sharp increase in inward interaction events and decrease in  
748 outward interaction events during the burn period, and fewer inward interaction events during the  
749 post-burn period than during the burn period but more numerous than during the pre-burn period.

750         The results of the quadrant analysis of momentum fluxes presented above are somewhat  
751 different from those of previous studies involving operational-scale prescribed burns. Heilman *et*  
752 *al.* (2021) showed that during an intense grass fire and two low-intensity forest understory fires,  
753 there can be substantial increase in the number and contribution of sweep and outward  
754 interaction events and that the increase in the positive momentum flux from outward interaction  
755 events largely offset the increase in the negative flux associated with sweep events. Whereas in  
756 the small fuel-bed scale burn here, inward interactions occur most frequently, followed by  
757 ejection events. However, the ejection event contributions to the mean momentum flux are larger  
758 (32.3%), with the inward interaction event contributions (24.2%) more similar to the outward  
759 interaction (23.4%) contributions. The feature of increased frequency of inward interaction  
760 events and their increased contribution to the mean momentum flux compared to previous burns  
761 is further observed in the post-burn period.

762         The event number and event contributions during the post-burn period also differ with  
763 increased ejection and inward interactions events, 32.8% and 20.6%, while the large-scale burns  
764 in Heilman *et al.* (2021) showed a closer return to pre-fire periods, with sweep and ejection  
765 events making up the majority of event number and contributions. The contributions from sweep,  
766 inward interaction, and ejection events remain elevated during the post-burn period, while the

767 contributions from outward interaction decrease during post-burn to values lower than the values  
768 of the pre-burn period.

769

#### 770 **4. Summary**

771 This study presents the atmospheric turbulence dynamics observed throughusing a  $4 \times 4$   
772 array of fast-response 3D sonic anemometers during a low-intensity fire experiment on a 10 m x  
773 10 m burn plot in the Silas Little Experimental Forest in New Jersey, USA. The density of  
774 turbulence measurements is unprecedented for fire experiments, allowing for a deeper analysis of  
775 heterogeneities as the surface line-fire spread through the burn plot than was previously possible.  
776 The analysis focuses on assessments of the fire impacts on turbulence intensity, as measured by  
777 *TKE*, turbulent momentum flux or shear stress as measured by friction velocity, and turbulent  
778 heat flux.

779 The influence of the low-intensity surface line-fire on the atmosphere above the  
780 combustion zone is evidenced by an increase in temperature up to 20 °C, the generation of strong  
781 updrafts up to  $6 \text{ m s}^{-1}$  and downdrafts up to  $-5 \text{ m s}^{-1}$  and a decrease in the streamwise velocity  
782 coupled with an increase in the cross-stream velocity indicating horizontal convergence in the  
783 vicinity of the fire front. The observed fire exhibited behavior more consistent with a buoyant  
784 plume than mechanically forced rising motion resulting from converging surface air. The  
785 influence of the fire on horizontal velocity components persisted longer after fire front passage  
786 while the influence on vertical velocity subsided rapidly behind the fire front.

787 The fire modified turbulence characteristics at the fuel bed-atmosphere interface. There  
788 was an increase in the turbulence intensity, with *TKE* values 2-3 times higher than the ambient

789 environment, due primarily to the increase in cross-stream velocity variance and, to a lesser  
790 degree, the increase in the vertical velocity and streamwise velocity variance. Heilman *et al.*  
791 (2017) also reported two to threefold increases in *TKE* values during two operational-scale low-  
792 intensity forest understory prescribed fires. It is interesting to note that this increase in *TKE* is  
793 only slightly smaller than what was observed during the intense grass fire during FireFlux  
794 (Clements *et al.*, 2007), although the magnitude of *TKE* of the intense grass fire is substantially  
795 larger than that of the low-intensity fires. Despite this increase in *TKE*, the value of *TKE* was still  
796 smaller than what is expected in an environment of substantial turbulence. Additionally, despite  
797 the increase in the vertical velocity variance during the fire, the *TKE* was still dominated by the  
798 horizontal velocity variance, indicating that the turbulence regime remained anisotropic  
799 (anisotropic ratio  $\ll 1/3$ ) above the combustion zone of this low-intensity fuel-bed-scale surface  
800 fire.

801         The fire enhanced upward sensible heat fluxes substantially by as much as 40 times the  
802 flux in the ambient atmosphere (from  $50 \text{ W m}^{-2}$  to  $2 \text{ kW m}^{-2}$ ). This change in the sensible heat  
803 flux is largely attributable to an increased contribution of upward transfer by turbulent eddies of  
804 warmer air from the combustion zone to the atmosphere above, which is also known as ejection  
805 events for vertical turbulent heat transfer. This increase in the contribution of the ejection events  
806 to turbulent heat fluxes was not caused by a corresponding increase in the number of ejection  
807 events that changed little from the pre-burn to burn periods. This mismatch between the ejection  
808 event contribution and event number suggests that the presence of a low-intensity fuel-bed-scale  
809 fire may not necessarily produce more upward turbulent heat transfer events, but rather, it can  
810 produce strong ejection events associated with large, energetic eddies. The warmer air

811 transported upward by the ejection events can also be transported downward by inward  
812 interaction events, which also increased somewhat during the fire.

813           Compared to the turbulent heat flux, the impact of the fire on turbulent momentum flux  
814 or shear stress was less pronounced. In general, an increase in momentum fluxes was observed  
815 during the burn, with friction velocity, a measure of total shear stress on horizontal wind, 2-3  
816 times the ambient value (from  $\sim 0.25 \text{ ms}^{-1}$  to  $0.6 \text{ ms}^{-1}$ ). Previous studies of operational-scale  
817 grass fire or forest understory fires also found up to a 3-fold increase in friction velocity despite  
818 that the scale of this fire is much smaller than the previous fires and that the absolute values of  
819 friction velocity during the intense grass fire were 5 times higher than the low-intensity fire here  
820 (Clements *et al.*, 2007; Heilman *et al.*, 2017; 2021). The fire was accompanied by an increase in  
821 the downward transfer of lower horizontal momentum air, also known as inward interaction  
822 events, along with a smaller increase in the upward transfer of lower horizontal momentum air  
823 referred to as ejection events. This finding differs from previous observations during an  
824 operational-scale forest understory fire where an increase in sweep (downward transfer of higher  
825 horizontal momentum air) and outward interaction (upward transfer of higher horizontal  
826 momentum air) contributions to the mean momentum fluxes were detected (Heilman *et al.*,  
827 2021).

828           These findings directly address the initial research inquiries: How does the surface fire  
829 impact turbulence intensity and the exchanges of turbulent heat and momentum between the  
830 combustion zone and the atmosphere above? Additionally, the investigation delves into whether  
831 and how the fire alters the distribution of heat and momentum fluxes into different event types,  
832 considering both event number and contribution.

833 Perhaps the most significant finding from this study is the large variations in the observed  
834 fire-induced perturbations across the sonic anemometer array in the burn plot. This directly  
835 corresponds to the third question raised in the introduction: How do the fire-induced  
836 modifications on turbulence vary spatially across the burn plot? The anemometers on the western  
837 side of the burn plot where a surface line-fire was ignited picked up very weak or no signals of  
838 the fire despite the proximity to the initial fire line. In contrast, the sonic anemometers in the  
839 center or eastern side of the burn plot picked up clear fire signals. Although the features of fire-  
840 induced turbulence regime (e.g., anisotropy, sweep-ejection dynamics) revealed by the sonic  
841 anemometers are similar, the magnitudes vary with downwind distance and the relative position  
842 of the sonic anemometers to the impinging fire front. Considering the size of the burn plot (10 m  
843 x 10 m) and the homogeneity of consumed fuels, this finding suggests that considerable care  
844 should be taken when comparing, contrasting, and combining data from multiple fires or from  
845 multiple instruments on the same fire to ensure that significant fire signals are not being over- or  
846 under-represented in the analyses that inform the conclusions of the studies. This also calls into  
847 question of using numerical simulations from coupled atmosphere-fire behavior models with  
848 horizontal grid spacing  $\geq 10$  m. The results presented here suggest that 1-2 m grid spacing is  
849 necessary for model simulations to capture atmospheric turbulent circulations that have  
850 spatiotemporal scales similar to the scales associated with flame dynamics in the combustion  
851 zone. It is however, impractical for operational applications to use such fine resolution.  
852 Operational models, with resolutions ranging from tens to hundreds of meters, often fall within  
853 the so called 'gray zone' where turbulence is partially resolved and existing turbulence closure  
854 schemes designed to parameterize all turbulent motions are inadequate. Advancements in  
855 computing technology have brought this zone to the forefront of operational model simulations.

856 Developing turbulence closure schemes for this scale is an active area of research. Large-eddy  
857 simulation (LES) models, validated using laboratory data, are instrumental in this endeavor. The  
858 experiments described in this study, capturing fire-induced turbulence on a 10 m x 10 m plot, can  
859 play a crucial role in developing turbulence parameterizations for the gray zone when combined  
860 with LES models.

861 Future work will compare results from this case with those of other burns in the SERDP  
862 10 m x 10 m fuel-bed-scale burn series to delineate the effect of fuel and ambient atmospheric  
863 conditions on fire-atmosphere interactions and with results from other prescribed-fire  
864 experiments to help scale up or scale down the results between small-scale and operational scale  
865 fires. Future work will also include the reanalysis of 10 Hz sonic anemometer data from other  
866 fire experiments using some or all of the methodologies employed here, which could contribute  
867 to the identification and documentation of a series of steps, protocols, standards, and  
868 methodologies by which 10-Hz sonic anemometer data collected during fire experiments can be  
869 compared and contextualized. Additionally, forthcoming analyses will integrate the data  
870 collected from the other instruments deployed during these ~~SERDP~~ fuel-bed-scale fire  
871 experiments. For instance, examining the high-frequency thermocouple vertical profile (0, 5, 10,  
872 20, 30, 50, 100 cm) in conjunction with infrared data can offer significant insights into the  
873 vertical variation of temperature between the combustion zone and the atmosphere immediately  
874 above should be included in future analyses. Finally yet importantly, employing Spectral and  
875 co-spectral analyses will be essential in revealing ~~should be performed to help understand~~ the  
876 temporal and spatial scale of turbulence regimes at the fuel-bed and atmosphere interface. These  
877 analyses will simultaneously enable a holistic exploration of the oscillatory behavior tied to line  
878 fires.



879 Another facet to delve into in future research involves the generation of vorticity, a  
880 consequential byproduct of fires that significantly influences fire behavior. Estimating fire-  
881 induced vorticity from field observations presents a formidable challenge, necessitating a  
882 carefully designed instrument array capable of capturing both horizontal and vertical variations  
883 in wind velocity. Despite these challenges, the utilization of the 4x4 sonic anemometer array in  
884 the 10m x 10m burn plot provides a distinctive opportunity. This array captures horizontal  
885 variations in wind velocity as the line fire spreads through the plot, offering a unique opportunity  
886 for estimating vertical vorticity associated with line fires. However, it is important to note that  
887 estimating horizontal vorticity is not feasible due to the sonic anemometer array's velocity  
888 measurement on a single vertical level (2.5 m), which does not capture the necessary vertical  
889 variations of velocity for horizontal vorticity calculation. Future experiments will require  
890 deploying a densely spaced sonic anemometer similar to the current one but at multiple vertical  
891 levels to comprehensively evaluate vorticity associated with fires.

892 Because the burn period was chosen to be between the time when the first and the last  
893 sonic anemometers have temperatures satisfying the threshold value (eight standard deviations in  
894 these analyses), the burn period included time after the fire has passed the sonic anemometer  
895 location, which likely yielded an underestimation of the fire effect. Similarly, the inclusion of all  
896 16 sonic anemometers in the analysis, including those that registered little fire signal, likely  
897 contributed to an underestimation. Consequently, fire-induced turbulent circulations and the  
898 associated turbulent heat and momentum fluxes are likely to be stronger than what has been  
899 reported here.

900

901 **Acknowledgements**

902 Founding for this project was provided by the U.S. Department of Defense Strategic  
903 Environmental Research and Development (SERDP) program (Project Number: RC-2461). We  
904 would like to acknowledge Jon Horn, Seoung-kyun Im, Robert Kremens, William Mell and  
905 Albert Simeoni for their contributions to the original research proposal. We thank Zach  
906 Campbell-Lochrie and Carlos Walker-Ravena for their help in the experiment design and  
907 instrument deployment of the 10 m x 10 m burn series. Our gratitude also extends to the two  
908 anonymous reviewers for their insightful and constructive comments, which have undeniably  
909 contributed to the enhancement of this manuscript.

910

#### 911 **Code and Data Availability**

912 Python language was used for all analyses and data management, with the Pandas package  
913 (<https://zenodo.org/record/7037953#.Yw-at3bMIp4>) used for data processing, NumPy package  
914 (<https://numpy.org/>) used for most statistical calculations and Matplotlib visualization package  
915 (<https://matplotlib.org/>) used for plotting, , all of which are open source packaged in the Python  
916 environment. The computer codes and the data are hosted on software sharing and version  
917 control website and service GitHub. [https://github.com/JosephSeitz/SERDP-10x10meter-Burn-](https://github.com/JosephSeitz/SERDP-10x10meter-Burn-Cleaner)  
918 [Cleaner.](https://github.com/JosephSeitz/SERDP-10x10meter-Burn-Cleaner)

919 All data used in this study are publicly archived and available via the USFS Data Archive (in  
920 press, links to be included in revised version).

921

#### 922 **Author Contributions**

923 All authors contributed to the research design. K.C., N.S., M.G., M.P., R.H. and E.M. conducted  
924 the fire experiment and collected the data. J.C. and M.P., with assistance from K.C., did the  
925 initial process and formatting of the data. J.S., with assistance and guidance from J.J.C. and  
926 discussions and feedback from S.Z., W.H., X.B. M.K., performed the data analysis and produced  
927 all the plots. S.Z. wrote the manuscript and was responsible for the revision. M.G., W.H., K.C.  
928 and N.S. edited the initial manuscript.

929

## References

- Amaya, M.A. and Clements C.B. (2020) Evolution of plume core structures and turbulence during a wildland fire experiment. *Atmosphere*, **11**, 842.
- Bennie, J., Huntley, B., Wiltshire, A., Hill, M.O. and Baxter, R. (2008) Slope, aspect and climate: Spatially explicit and implicit models of topographic microclimate in chalk grassland. *Ecological Modeling*, **216**, 47-59.
- Billmire, M., Frenc, N.H.F., Loboda, T., Owen, R.C. and Tyner, M. (2014) Santa Ana winds and predictors of wildfire progression in southern California, *International Journal of Wildland Fire*, **23**, 1119-1129.
- Calviño-Cancela, M, Chas-Amil, M.L., García-Martínez, E.D. and Touza, J. (2017) Interacting effects of topography, vegetation, human activities and wildland-urban interfaces on wildfire ignition risk. *Forest Ecology and Management*, **397**, 10-17.
- Campbell-Lochrie, Z., Walker-Ravena, C., Gallagher, M., Skowonski, N., Mueller, E., Hadden, R.M. (2021) Investigation of the role of bulk properties and in-bed structure in the flow regime of buoyancy-dominated flame spread in porous fuel bed. *Fire Safety Journal*, **120**, <https://doi.org/10.1016/j.firesaf.2020.103035>
- Campbell-Lochrie, Zakary J.; Hadden, Rory M.; Mueller, Eric V.; Walker-Ravena, Carlos; Gallagher, Michael R.; Clark, Kenneth L.; Hom, John L.; Kremens, Robert L.; Cole, Jason A.; Patterson, Matthew M.; Everland, Alexis I.; Skowronski, Nicholas S. 2022. Multi-scale analyses of wildland fire combustion processes: Small-scale field experiments -

Transportable Analyzer for Calorimetry Outside (TACO). Fort Collins, CO: Forest Service Research Data Archive.

Carrier, G.F., Fendell, F.E. and Wolff, M.F. (1991) Wind-aided fire spread across arrays of discrete fuel elements. I. Theory. *Combustion Science and Technology*, **75**, pp.31-51.

Clark, Kenneth L.; Gallagher, Michael R.; Mueller, Eric V.; Hadden, Rory M.; Walker-Ravena, Carlos; Campbell-Lochrie, Zakary J.; Cole, Jason A.; Patterson, Matthew M.; Everland, Alexis I.; Skowronski, Nicholas S. 2022a. Multi-scale analyses of wildland fire combustion processes: Small-scale field experiments - three-dimensional wind and temperature. Fort Collins, CO: Forest Service Research Data Archive.

Clark, Kenneth L.; Gallagher, Michael R.; Mueller, Eric V.; Hadden, Rory M.; Walker-Ravena, Carlos; Campbell-Lochrie, Zakary J.; Cole, Jason A.; Patterson, Matthew M.; Everland, Alexis I.; Skowronski, Nicholas S. 2022b. Multi-scale analyses of wildland fire combustion processes: Small-scale field experiments - temperature profile. Fort Collins, CO: Forest Service Research Data Archive.

Clark, K.L., Heilman, W.E., Skowronski, N.S., Gallagher, M.R., Mueller, E., Hadden, R.M., and Simeoni, A. (2020) Fire behavior, fuel consumption, and turbulence and energy exchange during prescribed fires in pitch pine forests. *Atmosphere*, **11**, 242.

Clark, T.L., Jenkins, M.A., Coen, J.L. and Packham, D.R., (1996) A coupled atmosphere-fire model: Role of the convective Froude number and dynamic fingering at the fireline. *International Journal of Wildland Fire*, **6**, pp.177-190.

Clements, C.B., and Seto, D. (2015) Observations of fire-atmosphere interactions and near-surface heat transport on a slope. *Boundary-Layer Meteorology*, **154**, 409-426.

- Clements, C.B., Kochanski, A.K., Seto, D., Davis, B., Camacho, C., Lareau, N.P., Contezac, J., Restaino, J., Heilman, W.E., Krueger, S.K. and Butler, B. (2019) The FireFlux II experiment: a model-guided field experiment to improve understanding of fire–atmosphere interactions and fire spread. *International Journal of Wildland Fire*, **28**, 308-326.
- Clements, C.B., Kochanski, A.K., Seto, D., Davis, B., Camacho, C., Lareau, N.P., Contezac, J., Restaino, J., Heilman, W.E., Krueger, S.K., Butler, B., Ottmar, R.D., Vihnanek, R., Flynn, J., Filippi, J.B., Barboni, T., Hall, D.E., Mandel, J., Jenkins, M.A., O'Brien, J., Hornsby, B., and Teske, C. (2019) The FireFlux II experiment: a model-guided field experiment to improve understanding of fire–atmosphere interactions and fire spread. *International Journal of Wildland Fire*, **28**, 308-326.
- Clements, C.B., Zhong, S., Bian, X., Heilman, W.E., and Byun, D.W. (2008), First observations of turbulence generated by grass fires. *Journal of Geophysical Research*, **113**, D22102.
- Clements, C.B., Zhong, S., Goodrick, S., Li, J., Potter, B.E., Bian, X., Heilman, W.E., Charney, J.J., Perna, R., Jang, M. and Lee, D. (2007) Observing the dynamics of wildland grass fires: FireFlux—A field validation experiment. *Bulletin of the American Meteorological Society*, **88**, 1369-1382.
- Di. Christina, G., Gallagher, M., Skowonski, N., Simeoni, In, S.-K. (2022) Design and implementation of a portable large-scale wind tunnel for wildfire research. *Fire Safety Journal*, **131**, 103607.
- Ebel, B.A. (2013) Simulated unsaturated flow processes after wildfire and interactions with slope aspect. *Water Resources Research*, **49**, 8090-8107

- Finney, M.A., Cohen, J.D., Forthofer, J.M., McAllister, S.S., Golner, M.J., Gorham, D.J., Saito, K., Akafuah, N.K., Adam, B.A., and English, J.D. (2015) Role of buoyant flame dynamics in wildfire spread. *Proceedings of the National Academy of Sciences*, **112**, 9833-9838.
- Forthofer, J.M., and Goodrick, S.L. (2011) Review of vortices in wildland fire. *Journal of Combustion*, **2011**, Article ID 984363.
- Gallagher, Michael R.; Skowronski, Nicholas S.; Hadden, Rory M.; Mueller, Eric V.; Clark, Kenneth L.; Campbell-Lochrie, Zakary J.; Walker-Ravena, Carlos; Kremens, Robert L.; Everland, Alexis I.; Patterson, Matthew M.; Cole, Jason A.; Heilman, Warren E.; Charney, Joseph J.; Bian, Xindi; Mell, William E.; Hom, John L.; Im, Seong-kyun; Kiefer, Michael T.; Zhong, Shiyuan; Simeoni, Albert J.; Rangwala, Ali; Di Cristina, Giovanni. (2022) Multi-scale analyses of wildland fire combustion processes: Small-scale field experiments – plot layout and documentation. Fort Collins, CO: Forest Service Research Data Archive
- Heilman, W.E. (2021) Atmospheric turbulence in wildland fire environments: implications for fire behavior and smoke dispersion. *Fire Management Today*. **79**, pp.24-29.
- Heilman, W.E. and Bian, X. (2013) Climate variability of near surface turbulent kinetic energy over the United States: Implications for fire weather prediction. *Journal of Applied Meteorology and Climatology*, **52**, 753-772.
- Heilman, W.E., Barnerjee, T., Clements, C.B., Clark, K.L., Zhong, S., and Bian X. (2021) Observations of sweep-ejection dynamics for heat and momentum fluxes during wildland fires in forested and grassland environments. *Journal of Applied Meteorology and Climatology*, **60**, 185-199.

- Heilman, W.E., Bian, X., Clark, K.L. and Zhong, S. (2019) Observations of turbulent heat and momentum fluxes during wildland fires in forested environments. *Journal of Applied Meteorology and Climatology*, **58**, pp.813-829.
- Heilman, W.E., Bian, X., Clark, K.L., Skowronski, N.S., Hom, J.L. and Gallagher, M.R. (2017) Atmospheric turbulence observations in the vicinity of surface fires in forested environments. *Journal of Applied Meteorology and Climatology*, **56**, 3133-3150.
- Heilman, W.E., Clements, C.B., Seto, D., Clark, K.L., Skowronski, N.S., and Hom, L.J. (2015) Observations of fire-induced turbulence regimes during low-intensity wildland fires in forested environments: Implications for smoke dispersion. *Atmospheric Science Letters*, **16**, 453-460.
- Heilman W.E. and Bian, X. (2013)
- Katul, G., Poggi, D., Cava, D., and Finnigan, J. (2006) The relative importance of ejections and sweeps to momentum transfer in the atmospheric boundary layer. *Bound.-Layer Meteor.*, **120**, 367–375.
- Katul, G., Kuhn, G., Schieldge, J., and Hsieh, C.-I. (1997) The ejection sweep character of scalar fluxes in the unstable surface layer. *Bound.-Layer Meteor.*, **83**, 1–26.
- Kitzberger, T., Falk, D.A., Westerling, A.L., and Swetnam T.W. (2017) Direct and indirect climate controls predict heterogeneous early-mid 21st century wildfire burned area across western and boreal North America. *PLOS ONE*, **12**, e0188486.
- Kremens, Robert L.; Gallagher, Michael R.; Clark, Kenneth L.; Mueller, Eric V.; Hadden, Rory M.; Heilman, Warren E.; Charney, Joseph J.; Hom, John L.; Campbell-Lochrie, Zakary J.;



- Walker-Ravena, Carlos; Everland, Alexis I.; Cole, Jason A.; Patterson, Matthew M.; Skowronski, Nicholas S. 2022. Multi-scale analyses of wildland fire combustion processes: Small-scale field experiments - fire radiative power. Fort Collins, CO: Forest Service Research Data Archive.
- Littell, J.S., Peterson, D.L., Riley, K.L., Liu, Y. and Luce, C.H. (2016). A review of the relationships between drought and forest fire in the United States. *Global Change Biology*, **22**, 2353-2369.
- Moody, M.J., Gibbs, J.A., Kruger, S., Mallia, D., Paradyjak, E.R., Kochanski, A.K., Bailey, B.N., Stoll, R. (2022) QES-Fire, a dynamically coupled fast-response wildfire model. *International Journal of Wildland Fire*, **31**, 306-325.
- Mueller, E.V., Skowronski, N., Clark, K., Gallagher, M., Kremens, R., Thomas, J.C., El Houssami, M., Filkov, A., Hadden, R.M., Mell, W.; et al. (2017) Utilization of remote sensing techniques for the quantification of fire behavior in two pine stands. *Fire Safety Journal*, **91**, 845–854, doi:10.1016/j.firesaf.2017.03.076.
- Potter, B.E. (1996) Atmospheric properties associated with large wildfires. *International Journal of Wildland Fire* **6**, 71–76.
- Potter, B.E. (2012): Atmospheric interactions with wildland fire behavior – I: Basic surface interactions, vertical profiles and synoptic structures. *International Journal of Wildland Fire*, **21**, 779-801.
- Povak, N.A., Hessburg, P.F. and Salter, R.B. (2018) Evidence for scale-dependent topographic controls on wildfire spread. *Ecosphere*, **9**(10): e02443.

- Seto, D., Strand, T.M., Clements, C.B., Thistle, H., and Mickler, R. (2014) Wind and plume thermodynamic structures during low-intensity subcanopy fires. *Agricultural and Forest Meteorology*, **198-199**, 53-61.
- Seto D., Clements, C.B., and Heilman, W.E. (2013) Turbulence spectra measured during fire front passage. *Agricultural and Forest Meteorology*, **169**, 195-210.
- Seto, D., and Clements, C.B. (2011) Fire whirl evolution observed during a valley wind-sea breeze reversal. *Journal of Combustion*, **2011**, 12pp <https://doi.org/10.1155/2011/569475>
- Sharples, J.J. (2009) An overview of mountain meteorological effects relevant to fire behaviour and bushfire risk. *International Journal of Wildland Fire* **18**, 737-754.
- Sharples, J.J., McRae, R.H.D., Wilkes, S.R. (2012) Wind–terrain effects on the propagation of wildfires in rugged terrain: Fire channelling. *International Journal of Wildland Fire*, **21**, 282-296.
- Skowronski, N.S. (2021) Multi-scale analysis of wildland fire combustion processes in open canopy forests using coupled iteratively informed laboratory-, field- and model-based approach. Final Technical Report, SERDP Project RC-2641. Available at <https://www.serdp-estcp.org/Program-Areas/Resource-Conservation-and-Resiliency/Air-Quality/Fire-Emissions/RC-2641>
- Skowronski, Nicholas S.; Charney, Joseph J; Clark, Kenneth L.; Gallagher, Michael R.; Hadden, Rory M.; Heilman, Warren E.; Hom, John L.; Kremens, Robert L.; Cole, Jason A.; Campbell-Lochrie, Zakary J.; Walker-Ravena, Carlos; Mueller, Eric V.; Everland, Alexis I.; Patterson, Matthew M. 2022a. Multi-scale analyses of wildland fire combustion

processes: Small-scale field experiments - infrared data. Fort Collins, CO: Forest Service Research Data Archive.

Skowronski, Nicholas S.; Charney, Joseph J; Clark, Kenneth L.; Gallagher, Michael R.; Hadden, Rory M.; Heilman, Warren E.; Hom, John L.; Kremens, Robert L.; Cole, Jason A.; Campbell-Lochrie, Zakary J.; Walker-Ravena, Carlos; Mueller, Eric V.; Everland, Alexis I.; Patterson, Matthew M. 2022b. Multi-scale analyses of wildland fire combustion processes: Small-scale field experiments – terrestrial laser scans. Fort Collins, CO: Forest Service Research Data Archive.

Skowronski, N., and Hom, J.L. (2015): Observations of fire-induced turbulence regimes during low-intensity wildland fires in forested environments: Implications for smoke dispersion. *Atmospheric Sciences Letters*, **16**, 453–460.

Stull, R.B., (1988) An introduction to boundary layer meteorology (Vol. 13). Springer Science & Business Media.

Viegas, D.X., and Neto, L.P. (1991) Wall shear stress as a parameter to correlate the rate of spread of a wind-induced forest fire. *International Journal of Wildland Fire*, **1**, 177–188.

Werth, P.A., Potter, B.E., Clements, C.B., Finney, M.A., Goodrick, S.L., Alexander, M.E., Cruz, M.G., Forthofer, J.A., and McAllister, S.S. (2011) Synthesis of knowledge of extreme fire behavior: For fire managers. General Technical Report PNW-GTR-854, US Department of Agriculture, Forest Service, Pacific Northwest Research Station, Vol. I. Portland, OR, 144.

Table 1. Vertical turbulent transfer events and the associated quadrat designations.

Q	$\phi'w'$	$\phi'$	$w'$	Heat flux	Momentum flux
1	>0	>0	>0	Ejection: upward flux of warmer air	Outward Interaction: upward flux of lower horizontal momentum air
2	<0	<0	>0	Inward Interaction: downward flux of warmer air	Sweep: downward flux of higher horizontal momentum air
3	>0	<0	<0	Sweep: downward flux of cooler air	Inward Interaction: downward flux of lower horizontal momentum air
4	<0	<0	>0	Outward Interaction: upward flux of cooler air	Ejection: upward flux of higher horizontal momentum air

## LIST OF FIGURES

Figure 1. Sketch of the burn plot and the instruments deployed to the plot. The four capital letters (A, B, C and D) denote the four trusses and the four numbers (1, 2, 3, 4) refer to the 3D sonic anemometers on the trusses. Posts hanging on trusses B and C show the heights and location of thermocouples. The center post indicates the position of the infrared camera. The boxes next to the sonic anemometers indicate the radiometer/spectral camera pairs. The rectangular box on the ground indicates fuel cells for fuel loading estimation. The symbol near B2 indicates the TACO for emission data collection

Figure 2. Surface meteorological condition on May 20, 2019, the day of the experimental burn, observed by the weather station approximately 200 m northeast of the burn plot.

Figure 3. Infrared images taken at 10 m above the center of the burn plot showing fuel bed temperature before a), near b) and after c-f) ignition.

Figure 4. Time series of 10-Hz observations of temperature ( $T$ ), horizontal wind speed ( $S$ ) and vertical wind component ( $w$ ) observed by the 16 sonic anemometers.

Figure 5. The number of sonic anemometers that recorded temperatures at or above a given threshold value (left) and the length of period over which the threshold was reached or exceeded (right). The symbol  $\sigma$  denotes pre-burn period temperature standard deviation.

Figure 6. Time series of 10 Hz streamwise ( $u$ , blue) and cross-stream ( $v$ , green) wind velocity components and temperature perturbations ( $T'$ , red) recorded by each sonic anemometer at 2.5 m above the ground. The vertical dashed black lines indicate the burn period determined by the first and last occurrence of  $T' \geq 8\sigma$ . Time is the minutes since the start of the pre-burn period.

Figure 7. Distributions of 10 Hz streamwise ( $u$ ), cross-stream ( $v$ ), and vertical ( $w$ ) wind velocity components, and temperature perturbations ( $T'$ ) from all 16 sonic anemometers during pre-burn, burn and post-burn periods. The box represents the 25<sup>th</sup> and 75<sup>th</sup> percentile of the data, with data inside the whiskers representing 99.3% of the data. The orange line in the boxes is the median value, the green triangle is the mean, and the blue shading is the density of values of the data.

Figure 8. Time series of 1-minute averaged turbulent kinetic energy ( $TKE$ ) (red) for each sonic anemometer and the three components of velocity variance,  $u'^2/2$  (yellow),  $v'^2/2$  (blue) and  $w'^2/2$  (green), that make up the  $TKE$ . The vertical dashed black lines indicate the burn period determined by the first and last occurrence of  $T' \geq 8\sigma$ . Time is the minutes since the start of the pre-burn period.

Figure 9. Distributions of turbulent kinetic energy ( $TKE$ ) and the three components of velocity variance ( $u'^2/2$ ,  $v'^2/2$  and  $w'^2/2$ ) that make up the  $TKE$  from all 16 sonic anemometers during the pre-burn, burn and post-burn periods. The box represents the 25<sup>th</sup> and 75<sup>th</sup> percentile of the data, with data inside the whiskers representing 99.3% of the data. The orange line in the boxes is the median value, the green triangle is the mean, and the blue shading is the density of values of the data.

Figure 10. Time series of 1-minute averaged friction velocity squared ( $u_*^2$ , pink pluses) and its two components, the streamwise kinematic momentum flux,  $\overline{u'w'}$  (yellow circle) and the cross-stream kinematic momentum flux,  $\overline{v'w'}$  (blue diamonds), for each of the 16 sonic anemometers. The vertical dashed black lines indicate the burn period determined by the first and last occurrence of  $T' \geq 8\sigma$ . Time is the minutes since the start of the pre-burn period.

Figure 11. Distributions of friction velocity squared ( $u_*^2$ ) and its two components ( $\overline{u'w'}$  and  $\overline{v'w'}$ ) from all 16 sonic anemometers during the pre-burn, burn, and post-burn periods. The box represents the 25<sup>th</sup> and 75<sup>th</sup> percentile of the data, with data inside the whiskers representing 99.3% of the data. The orange line in the boxes is the median value, the green triangle is the mean, and the blue shading is the density of values of the data.

Figure 12. Time series of 1-minute averaged heat flux for each of the 16 sonic anemometers (left) and the distribution of heat fluxes from all 16 sonic anemometers during the pre-burn, burn, and post-burn periods (right). The box represents the 25<sup>th</sup> and 75<sup>th</sup> percentile of the data, with data inside the whiskers representing 99.3% of the data. The orange line in the boxes is the median value, the green triangle is the mean, and the blue shading is the density of values of the data.

Figure 13. Quadrant analysis of the instantaneous vertical kinematic turbulent heat fluxes showing the contributions to the total flux from (top row), and the percent of (bottom row) the four types of events: outward interaction (green), ejection (red), inward interaction (blue), and sweep (orange) for each of the 16 sonic anemometers during the pre-burn, burn, and post-burn periods. The black diamonds in the top row indicate the total heat flux values. The sonic anemometers are arranged from west to east roughly following the fire spread across the burn plot.

Figure 14. Quadrant analysis of the instantaneous vertical kinematic turbulent heat fluxes showing the contributions to the total flux from (top row), and the percent of (bottom row) the four types of events: outward interaction (green), ejection (red), inward interaction (blue), and sweep (orange) for all 16 sonic anemometers during the pre-burn, burn, and post-burn periods. The black diamonds in the top row indicate the total heat flux values. The sonic anemometers are arranged from west to east roughly following the fire spread across the burn plot.

Figure 15. Quadrant analysis of the instantaneous vertical kinematic turbulent fluxes of horizontal momentum showing the contributions to the total flux from (top row), and the percent of (bottom row) the four types of events: outward interaction (red), sweep (green), inward interaction (orange), and ejection (blue) for each of the 16 sonic anemometers during the pre-burn, burn, and post-burn periods. The black diamonds in the top row indicate the total flux values. The sonic anemometers are arranged from west to east roughly following the fire spread across the burn plot.

Figure 16. Quadrant analysis of the instantaneous vertical kinematic turbulent fluxes of horizontal momentum showing the contributions to the total flux from (top row), and the percent of (bottom row) the four types of events: outward interaction (red), sweep (green), inward

interaction (orange), and ejection (blue) for all 16 sonic anemometers during the pre-burn, burn, and post-burn periods. The black diamonds in the top row indicate the total flux values. The sonic anemometers are arranged from west to east roughly following the fire spread across the burn plot.

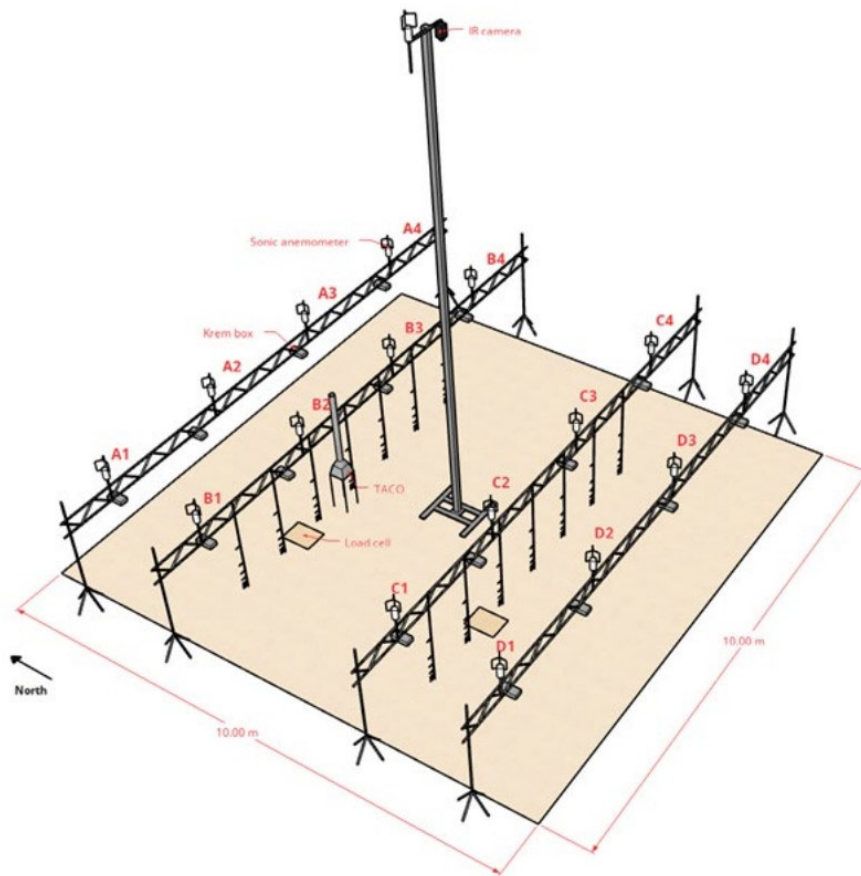


Figure 1. Sketch of the burn plot and the instruments deployed to the plot. The four capital letters (A, B, C and D) denote the four trusses and the four numbers (1, 2, 3, 4) refer to the 3D sonic anemometers on the trusses. Posts hanging on trusses B and C show the heights and location of thermocouples. The center post indicates the position of the infrared camera. The boxes next to the sonic anemometers indicate the radiometer/spectral camera pairs. The rectangular box on the ground indicates fuel cells for fuel loading estimation. The symbol near B2 indicates the TACO for emission data collection



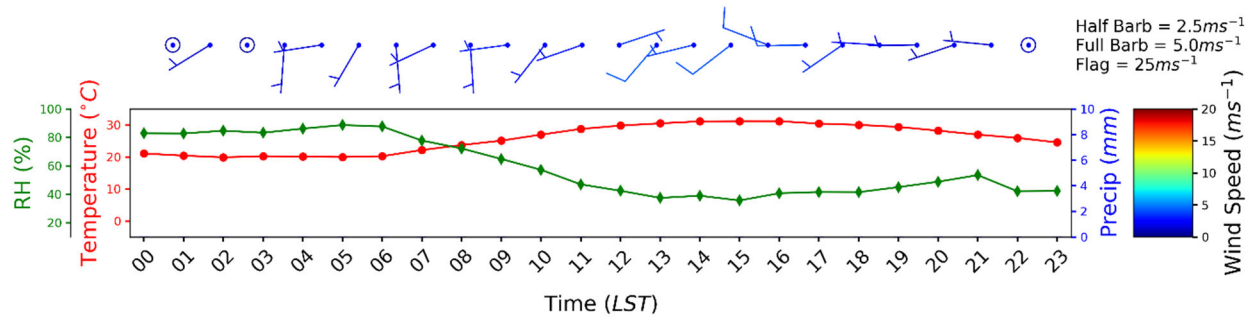


Figure 2. Surface meteorological condition on May 20, 2019, the day of the experimental burn, observed by the weather station approximately 200 m northeast of the burn plot.

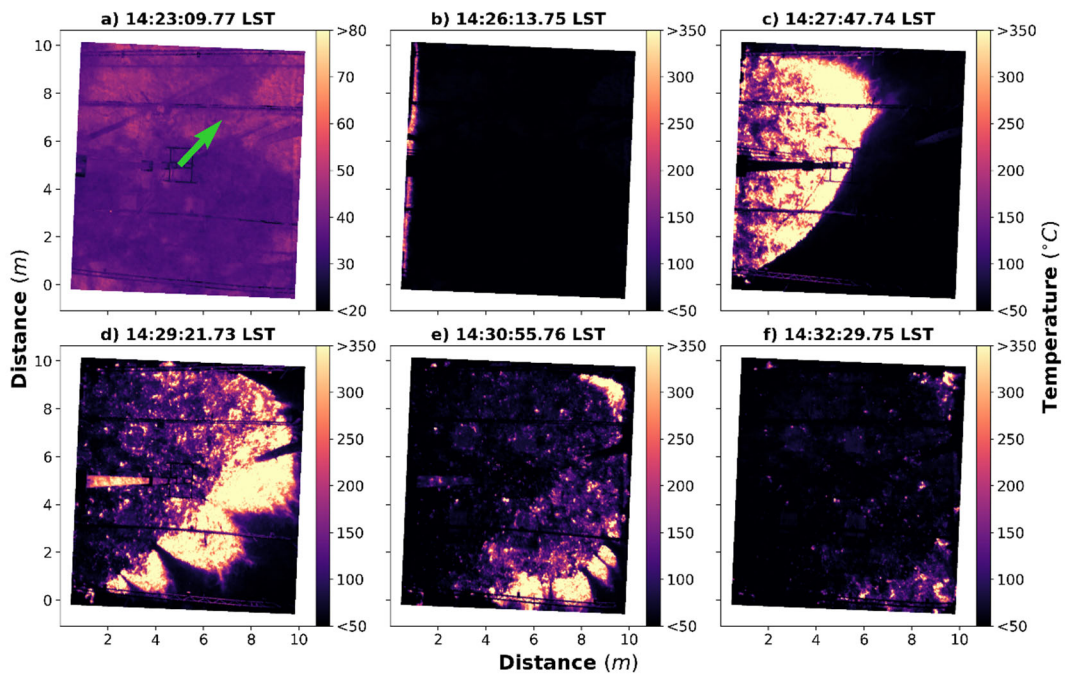


Figure 3. Infrared images taken at 10 m above the center of the burn plot showing fuel bed temperature before a), near b) and after c-f) ignition. The green arrow indicates the direction of background wind.

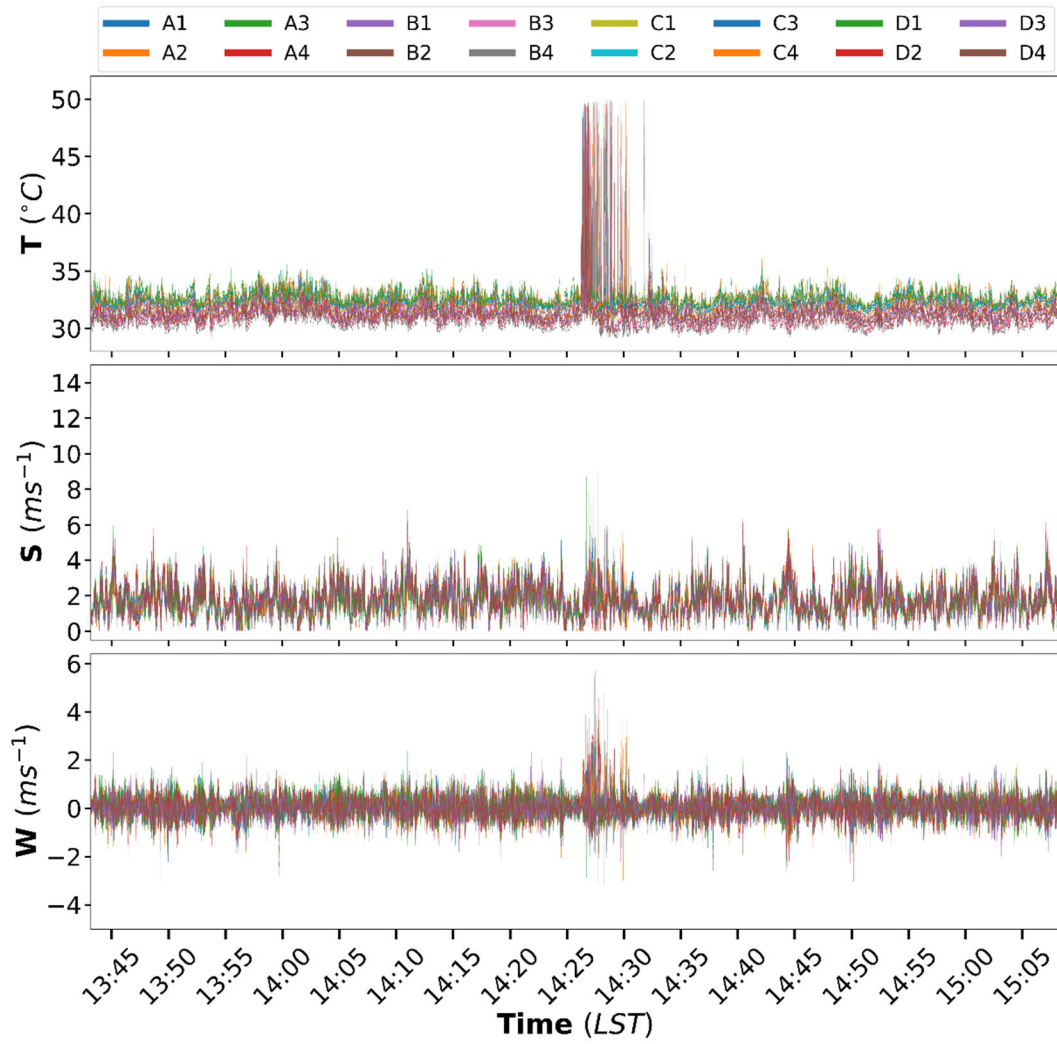


Figure 4. Time series of 10-Hz observations of temperature ( $T$ ), horizontal wind speed ( $S$ ) and vertical wind component ( $w$ ) observed by the 16 sonic anemometers.

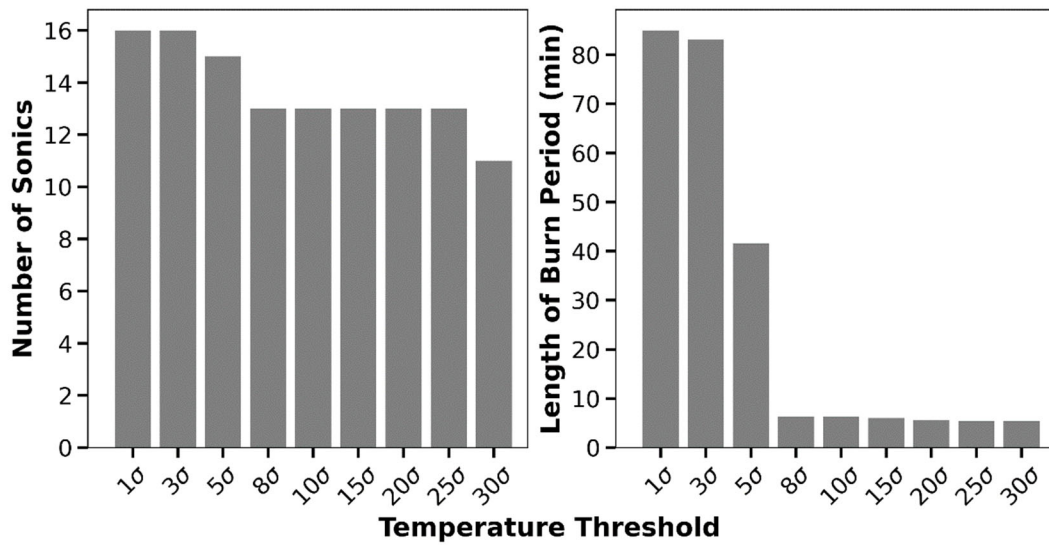


Figure 5. The number of sonic anemometers that recorded temperatures at or above a given threshold value (left) and the length of period over which the threshold was reached or exceeded (right). The symbol  $\sigma$  denotes pre-burn period temperature standard deviation.

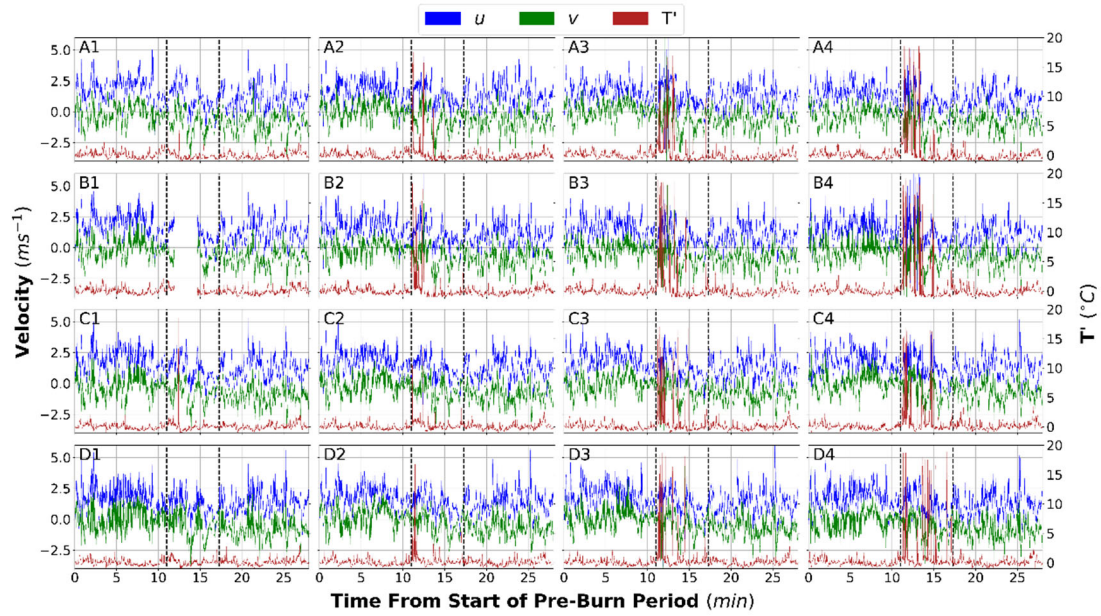


Figure 6. Time series of 10 Hz streamwise ( $u$ , blue) and cross-stream ( $v$ , green) wind velocity components and temperature perturbations ( $T'$ , red) recorded by each sonic anemometer at 2.5 m above the ground. The vertical dashed black lines indicate the burn period determined by the first and last occurrence of  $T' \geq 8\sigma$ . Time is the minutes since the start of the pre-burn period.

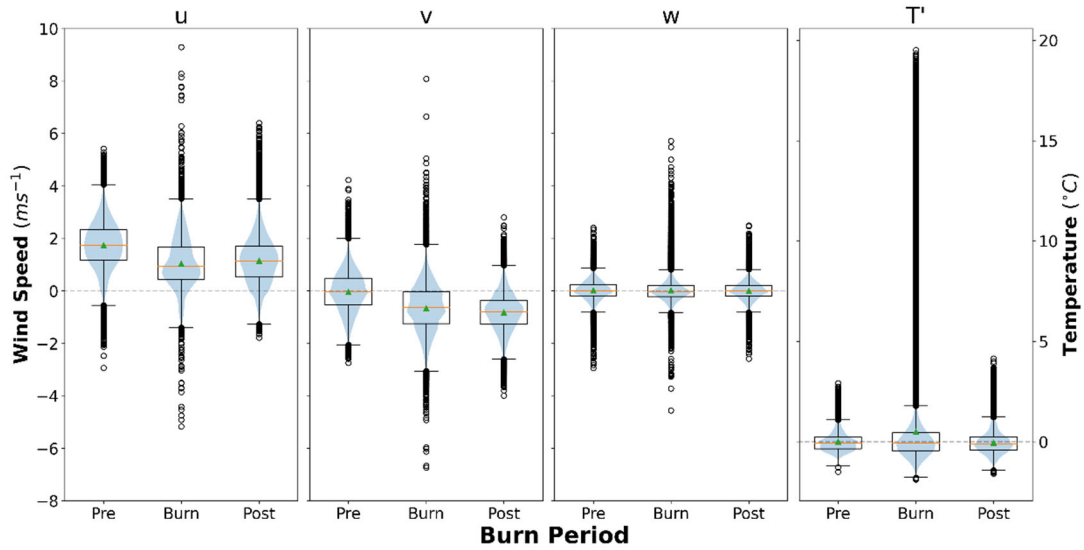


Figure 7. Distributions of 10 Hz streamwise ( $u$ ), cross-stream ( $v$ ), and vertical ( $w$ ) wind velocity components, and temperature perturbations ( $T'$ ) from all 16 sonic anemometers during pre-burn, burn and post-burn periods. The box represents the 25<sup>th</sup> and 75<sup>th</sup> percentile of the data, with data inside the whiskers representing 99.3% of the data. The orange line in the boxes is the median value, the green triangle is the mean, and the blue shading is the density of values of the data.

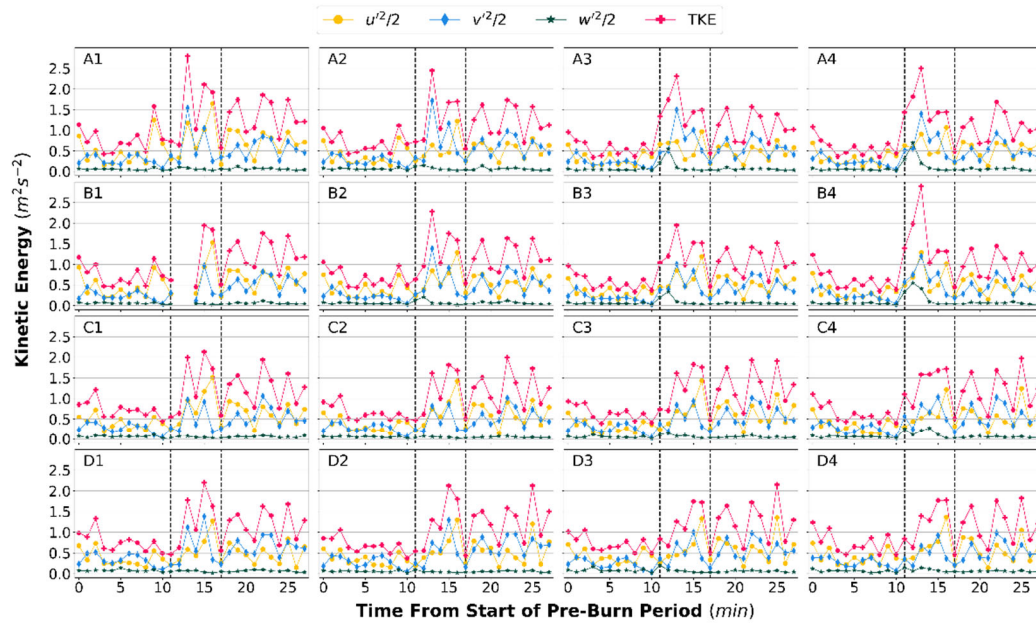


Figure 8. Time series of 1-minute averaged turbulent kinetic energy ( $TKE$ ) (red) for each sonic anemometer and the three components of velocity variance,  $u'^2/2$  (yellow),  $v'^2/2$  (blue) and  $w'^2/2$  (green), that make up the  $TKE$ . The vertical dashed black lines indicate the burn period determined by the first and last occurrence of  $T' \geq \delta\sigma$ . Time is the minutes since the start of the pre-burn period

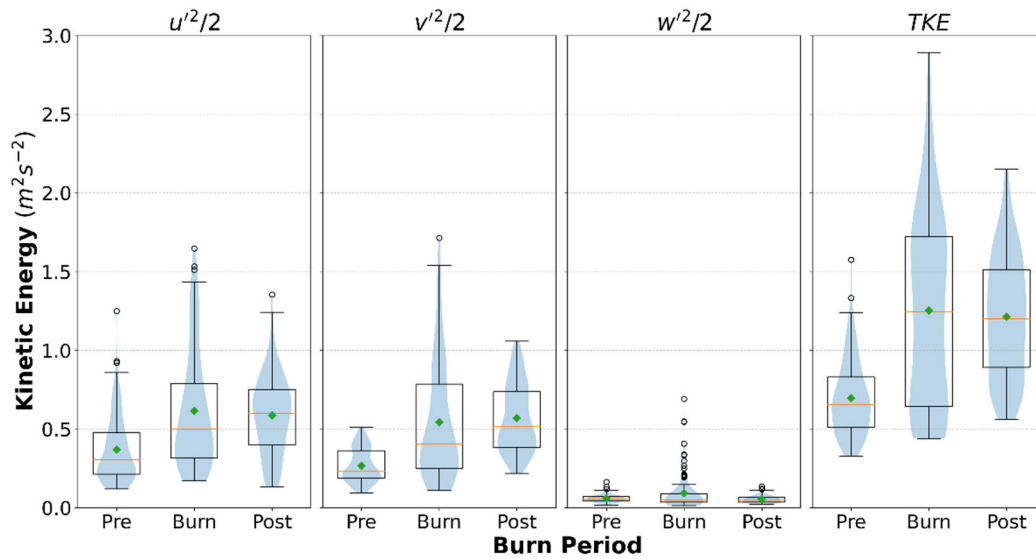


Figure 9. Distributions of turbulent kinetic energy ( $TKE$ ) and the three components of velocity variance ( $u'^2/2$ ,  $v'^2/2$  and  $w'^2/2$ ) that make up the  $TKE$  from all 16 sonic anemometers during the pre-burn, burn and post-burn periods. The box represents the 25<sup>th</sup> and 75<sup>th</sup> percentile of the data, with data inside the whiskers representing 99.3% of the data. The orange line in the boxes is the median value, the green triangle is the mean, and the blue shading is the density of values of the data.



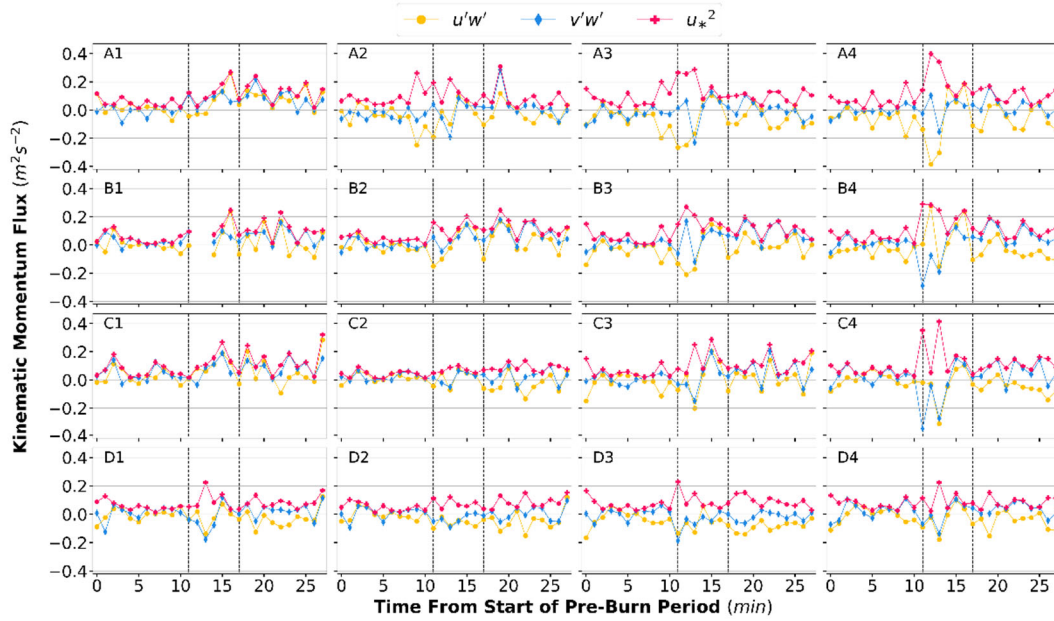


Figure 10. Time series of 1-minute averaged friction velocity squared ( $u_*^2$ , pink pluses) and its two components, the streamwise kinematic momentum flux,  $\overline{u'w'}$  (yellow circle) and the cross-stream kinematic momentum flux,  $\overline{v'w'}$  (blue diamonds), for each of the 16 sonic anemometers. The vertical dashed black lines indicate the burn period determined by the first and last occurrence of  $T' \geq 8\sigma$ . Time is the minutes since the start of the pre-burn period.

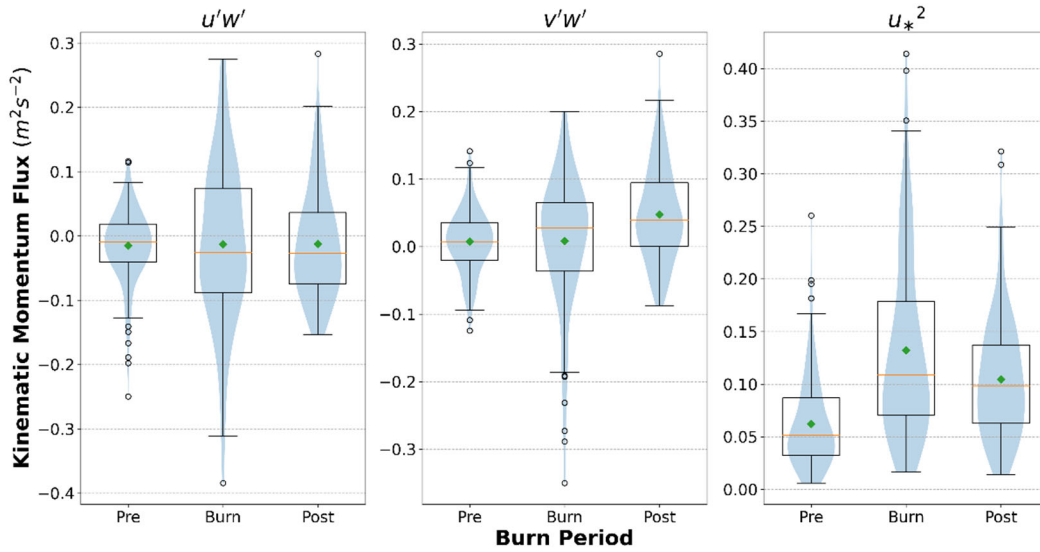


Figure 11. Distributions of friction velocity squared ( $u_*^2$ ) and its two components ( $\overline{u'w'}$  and  $\overline{v'w'}$ ) from all 16 sonic anemometers during the pre-burn, burn, and post-burn periods. The box represents the 25<sup>th</sup> and 75<sup>th</sup> percentile of the data, with data inside the whiskers representing 99.3% of the data. The orange line in the boxes is the median value, the green triangle is the mean, and the blue shading is the density of values of the data.

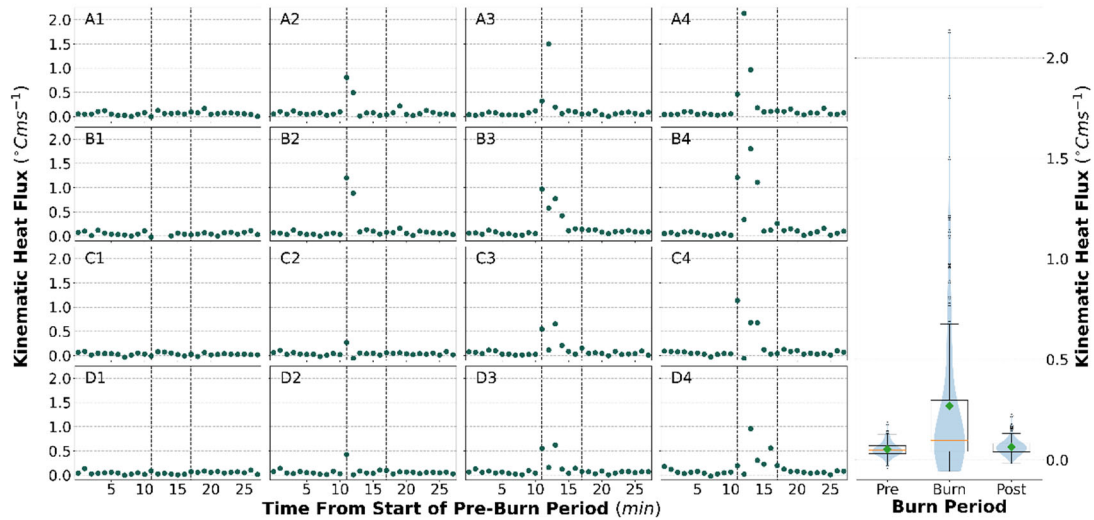


Figure 12. Time series of 1-minute averaged heat flux for each of the 16 sonic anemometers (left) and the distribution of heat fluxes from all 16 sonic anemometers during the pre-burn, burn, and post-burn periods (right). The box represents the 25<sup>th</sup> and 75<sup>th</sup> percentile of the data, with data inside the whiskers representing 99.3% of the data. The orange line in the boxes is the median value, the green triangle is the mean, and the blue shading is the density of values of the data.

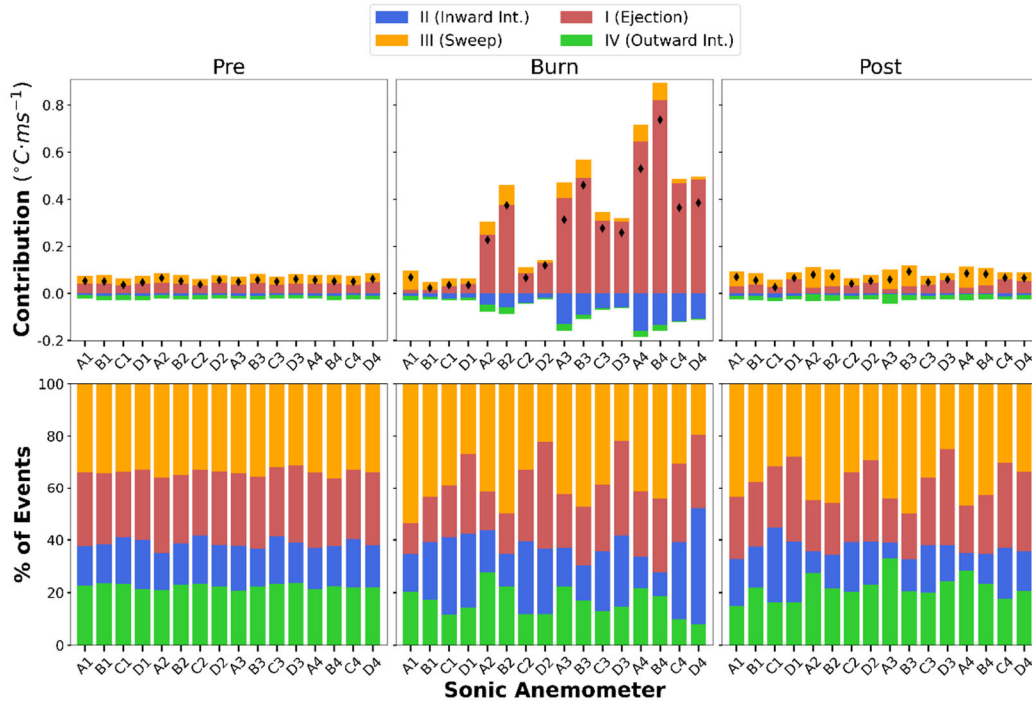


Figure 13. Quadrant analysis of the instantaneous vertical kinematic turbulent heat fluxes showing the contributions to the total flux from (top row), and the percent of (bottom row) the four types of events: outward interaction (green), ejection (red), inward interaction (blue), and sweep (orange) for each of the 16 sonic anemometers during the pre-burn, burn, and post-burn periods. The black diamonds in the top row indicate the total heat flux values. The sonic anemometers are arranged from west to east roughly following the fire spread across the burn plot.

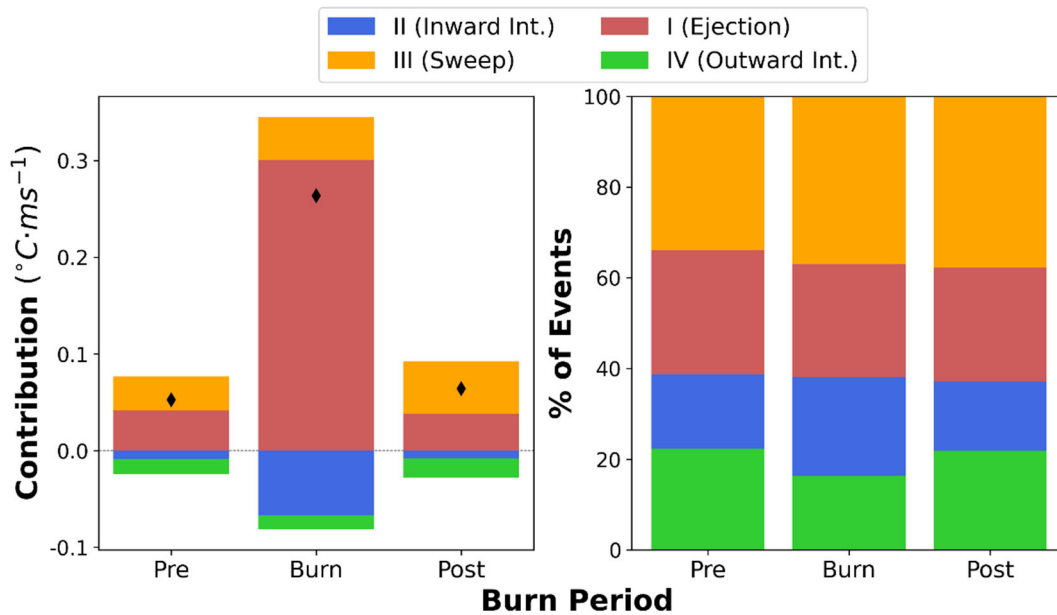


Figure 14. Quadrant analysis of the instantaneous vertical kinematic turbulent heat fluxes showing the contributions to the total flux from (top row), and the percent of (bottom row) the four types of events: outward interaction (green), ejection (red), inward interaction (blue), and sweep (orange) for all 16 sonic anemometers during the pre-burn, burn, and post-burn periods. The black diamonds in the top row indicate the total heat flux values. The sonic anemometers are arranged from west to east roughly following the fire spread across the burn plot.

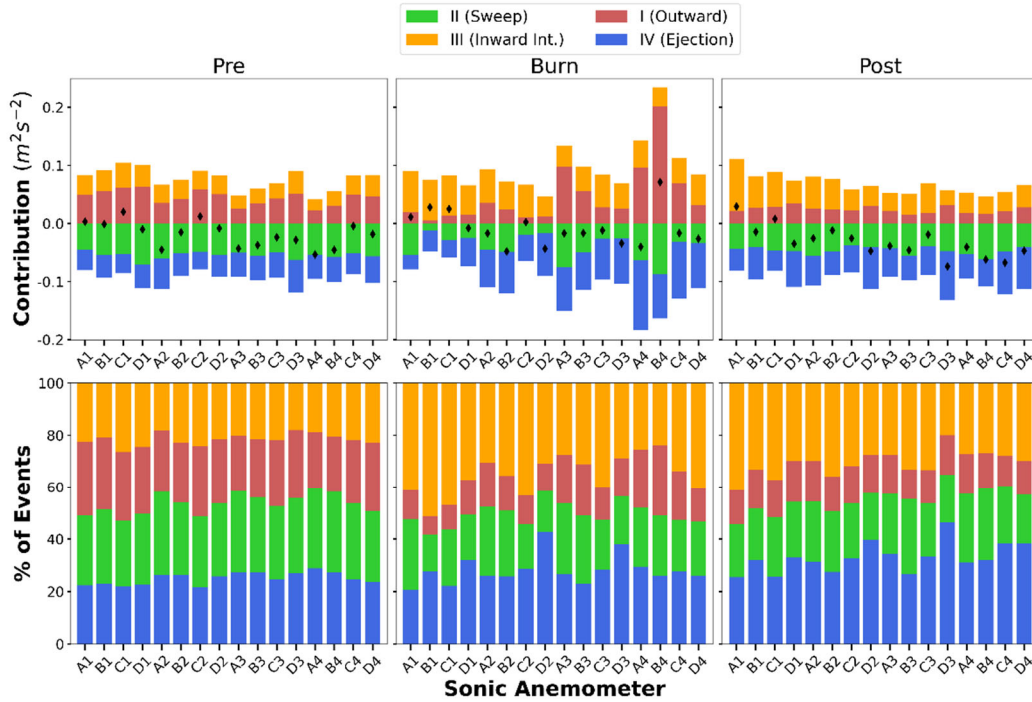


Figure 15. Quadrant analysis of the instantaneous vertical kinematic turbulent fluxes of horizontal momentum showing the contributions to the total flux from (top row), and the percent of (bottom row) the four types of events: outward interaction (red), sweep (green), inward interaction (orange), and ejection (blue) for each of the 16 sonic anemometers during the pre-burn, burn, and post-burn periods. The black diamonds in the top row indicate the total flux values. The sonic anemometers are arranged from west to east roughly following the fire spread across the burn plot.

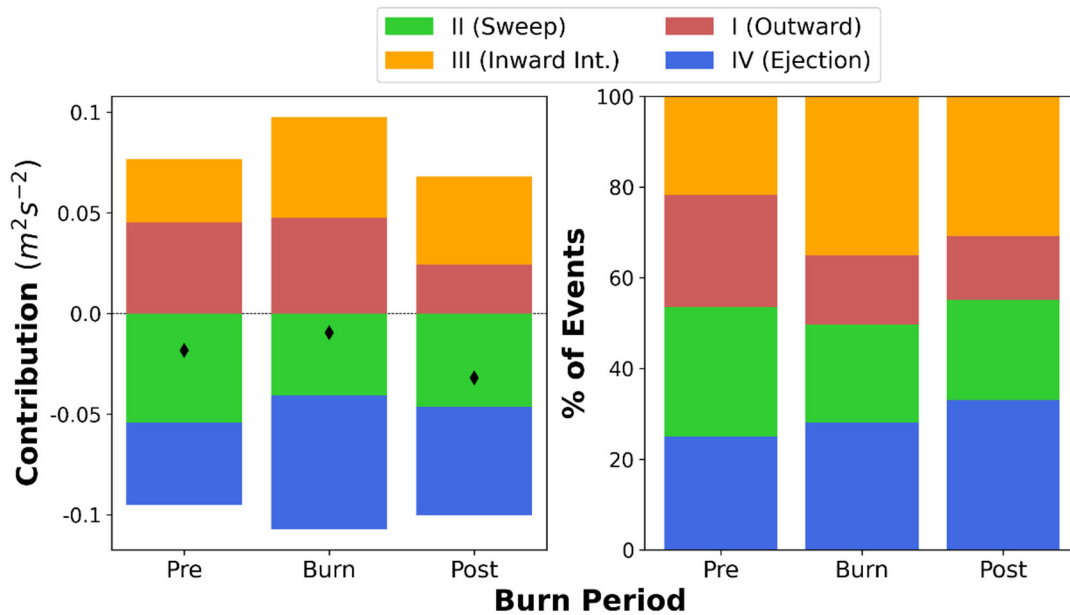


Figure 16. Quadrant analysis of the instantaneous vertical kinematic turbulent fluxes of horizontal momentum showing the contributions to the total flux from (top row), and the percent of (bottom row) the four types of events: outward interaction (red), sweep (green), inward interaction (orange), and ejection (blue) for all 16 sonic anemometers during the pre-burn, burn, and post-burn periods. The black diamonds in the top row indicate the total flux values. The sonic anemometers are arranged from west to east roughly following the fire spread across the burn plot.